geosciences

MDPI

Article

Photogrammetric Prediction of Rock Fracture Properties and Validation with Metric Shear Tests

Lauri Uotinen [1,*], Masoud Torkan [1], Alireza Baghbanan [2], Enrique Caballero Hernández [3] and Mikael Rinne [1]

1 Department of Civil Engineering, School of Engineering, Aalto University, FI-02150 Espoo, Finland; masoud.torkan@aalto.fi (M.T.); mikael.rinne@aalto.fi (M.R.)
2 Department of Mining Engineering (DME), Isfahan University of Technology (IUT), Isfahan 84156-83111, Iran; bagh110@cc.iut.ac.ir
3 Stress Measurement Company Oy, FI-00180 Helsinki, Finland; enrique.caballero@smcoy.fi
* Correspondence: lauri.uotinen@aalto.fi

Abstract: An accurate understanding of jointed rock mass behavior is important in many applications ranging from deep geological disposal of nuclear waste, to deep mining, and to urban geoengineering projects. The roughness of rock fractures and the matching of the fracture surfaces are the key contributors to the shear strength of rock fractures. In this research, push shear tests with three normal stress levels of 3.6, 6.0, and 8.5 kPa were conducted on two granite samples with artificially induced well-matching tensile fractures with sizes of 500 mm × 250 mm and 1000 mm × 500 mm. The large sample reached on average a −60% weaker peak shear stress than the medium-sized sample, and a strong negative scale effect was observed in the peak shear strength. The roughness of the surfaces was measured using a profilometer and photogrammetry. The scale-corrected profilometer-based method (joint roughness coefficient, JRC) underestimates the peak friction angle for the medium-sized slabs by −27% for the medium sample and −9% for the large sample. The photogrammetry-based (Z'_2) method produces an estimate with −7% (medium) and + 12% (large) errors. The photogrammetry-based Z'_2 is an objective method that consistently produces usable estimates for the JRC and peak friction angle.

Keywords: shear test; scale effect; roughness; photogrammetry; friction angle

Citation: Uotinen, L.; Torkan, M.; Baghbanan, A.; Hernández, E.C.; Rinne, M. Photogrammetric Prediction of Rock Fracture Properties and Validation with Metric Shear Tests. *Geosciences* **2021**, *11*, 293. https://doi.org/10.3390/geosciences11070293

Academic Editors: Gessica Umili, Anna Maria Ferrero, Maria Migliazza and Jesus Martinez-Frias

Received: 29 May 2021
Accepted: 5 July 2021
Published: 15 July 2021

1. Introduction

The roughness of rock joints and the matedness of the joint surfaces are key contributors to the shear strength of rock joints. For a jointed rock mass, in addition to the intact material strength, the strength of the rock mass is influenced by the orientation, geometry, roughness, and matedness of the rock joints. An accurate understanding of jointed rock mass behavior is important in many applications ranging from deep geological disposal of nuclear waste to deep mining to geoengineering projects below urban environments.

Understanding shear joint behavior depends on diverse parameters, including normal stress [1], the size and scale of the joint [2,3], the roughness of the joint surface [4,5], matedness [6,7], mineral composition [8], surface condition (e.g., dry, wet, submerged, weathered, unweathered) [9–11], and mechanical properties (e.g., the friction angle, compressive strength of the joint wall, etc.) [5]. Joint roughness and the roughness scaling of all these parameters play key roles in the stability of rock excavations since they influence the mechanical and hydraulic behaviors of the rock mass [5,12,13].

The scale effect is significant, as it affects shear tests and the measurement resolution of joint roughness coefficient (JRC). The JRC is used to show the degree of roughness [5,13]. In most cases, there seems to be a lack of unanimous agreement on the effects of the sample size on shear strength. As Bandis et al. [3] affirm, the majority of the cases fail to yield a concrete conclusion as to whether this effect on shear strength is negative, positive, or neutral.

An explanation for the observed, usually negative, scale effect for the peak shear strength of rock joints was given in [14]. The term matedness describes how much of the fracture surfaces are in good contact with each other. The conceptual model for peak strength of rock joints depends on the matedness of rock joints; if the fracture surfaces are well matched, the negative scale effect of peak shear strength associated with larger rock joint surfaces should not occur and the strength is independent of the fracture size. Otherwise, a scale effect might be detected. To test this hypothesis in large scale, two push shear tests were conducted for fresh well mated rock joints in unweathered granite samples. To detect any scale effects, two samples were selected: a large sample 2000 mm × 1000 mm × 130 mm and a medium sample 500 mm × 250 mm × 45 mm. If no change in the shear stress is observed, then the Johansson model fits the data better [14]. The consensus is that a negative scale effect of shear stress should be observed. Using the formula for shear strength from [3], it can be estimated that the peak strength for the 2 m sample compared to the 0.5 m sample should drop by approximately −33%. The estimate was calculated using the uniaxial compressive strength 187 MPa as the estimate for joint compressive strength and basic friction angle of 33° as the estimate for residual friction angle.

One of the most common ways to measure the roughness of a rock joint is to use a profilometer to capture a two-dimensional curve of the surface, compare it visually to a set of reference curves, and then select the best matching value [5]. Roughness could affect the mechanical properties of joints, such as the peak friction angle and the peak shear strength [15]. Some formulae, such as linear [15] and polynomial [16,17], have been introduced to approximate the peak friction angle based on JRC values. The matedness of the joint surfaces is usually not considered when assessing the shear strength of rock joints. The measurement of roughness is prone to human errors in conducting the measurement. A subjective choice is made in visual comparison of the measured curve to the reference curves and in the selection of the best matching JRC value. In this research, it is shown how photogrammetry can be used to obtain objective measurements of the rock joint roughness. The proposed method is compared to the visual assessment. Finally, the accuracy of the predictions for peak friction angles is compared to shear tests conducted for artificial fractures with sizes of 2 m × 1 m and 0.50 m × 0.25 m. The direct shear test is the most reliable method for assessing the peak friction angle as it gives direct observations, although it is time-consuming and costly.

Different methods are used to characterize roughness, such as statistical [18–22], fractal [22,23], and directional methods. Roughness properties which have been characterized by directional methods feature a wide variety of techniques, namely: (1) contact methods, for instance a profilometer [5] and a stylus profilometer [23]; (2) atomic force microscopy [24], and (3) non-invasive optical techniques, for example, shadow edge [19], 3D laser scanning [25], confocal microscopy [26], white-light interferometry [27], laser triangulation [28], light detection and ranging (LiDAR) [29,30], a fringe projection stereo camera [31–33], and photogrammetry as an optical method [34–53]. Among these methods, photogrammetry, as a precise measurement [35,41], can not only be used to evaluate properties of roughness, for instance, the friction angle [46–49], but is also employed to reconstruct the 3D surface of roughness [41,54].

Roughness scaling has a widely-observed impact on joint shear as reported in [3,5,14,55–60]. The results of extensive studies of the scale effects have been summarized in a number of recent research studies [56,57,60,61].

The equations by Barton and Choubey [5] for the prediction of joint shear strength yield insufficiently accurate estimations for large-scale conditions [20]. Measurement conditions for the scale effect are also important [13,62]. Consequently, the discussion of the effect of the sample size on the shear strength is still unsettled.

2. Methodology

2.1. Overview of the Research Methods Used

This work was conducted as follows (1) Preparation of rock samples: One large-scale slab (2.000 m × 1.000 m × 0.130 m) and one medium-scale slab (0.500 m × 0.250 m × 0.045 m), with horizontal artificial fractures. (2) Evaluation of fracture surface roughness using a profilometer and Barton and Choubey profiles. (3) Preparation of 3D photogrammetry-based models of the rock samples. (4) Calculation of JRC values by statistical methods from the 3D models. (5) Shear testing of the rock samples. (6) Evaluation and comparison of the results. (7) Comparison of the results from the tests.

2.2. Manufacturing of the Slab Pairs

The rock samples originate from intact Finnish Kuru grey granite blocks [63]. The rock fracture was induced by drilling short holes in the perimeter of the rock block and by splitting the slab by applying tensile stress using plugs, the so-called plug and feather technique. Defects of the rock block were detected based on the mine crew's experience to select the best direction for drilling. Holes placed 15 cm away from each other were drilled along a line representing a projected crack. Afterward, 10 cm plug and feather sets were embedded in the holes in such a way that the direction of the feathers' ears was perpendicular to the projected cracks. Subsequently, the plugs were gradually hammered into the holes with a rubber hammer. After observing an initial crack, the fracture direction indicates which plug should be hammered to next. After the crack has propagated throughout the whole rock block, the two parts of the rocks were split with a wrench. After splitting, the rock blocks were cut to the desired dimensions (2000 mm × 1000 mm × 130 mm and 500 mm × 250 mm × 45 mm).

2.3. Surface Roughness Measurements

The roughness of the fracture surfaces was measured in two ways. In the contact method, the JRC values were approximated by comparing the profiles defined by the profilometer with Barton and Choubey's standard profiles [5]. The second approach utilized the profiles obtained through digitalization of the fracture surfaces. The JRC values (JRC_i) obtained by both methods for each section (i) were averaged to calculate the final JRC value for each fracture surface (Equation (1))

$$JRC = \frac{1}{n} \sum_{i=1}^{n} JRC_i, \quad (1)$$

2.3.1. Roughness Measurements Using the Profilometer

As shown in Figure 1, three lines in the planned shearing direction along Y-axis were drawn to measure the roughness of the slabs' surfaces. For the large sample, the lines are spaced at 250 mm intervals along the X-axis, while for the medium sample at 62.5 mm intervals. The photographed profilometer profiles were assigned every 10 cm, the JRC value was assessed and compared with the Barton and Choubey standard profiles [5].

Mapping scratched points from shear tests in different stages was accomplished through visual observation and with a ruler. The criterion used to define damage was shear or scratch marks on the surface, such as dust or debris of granite.

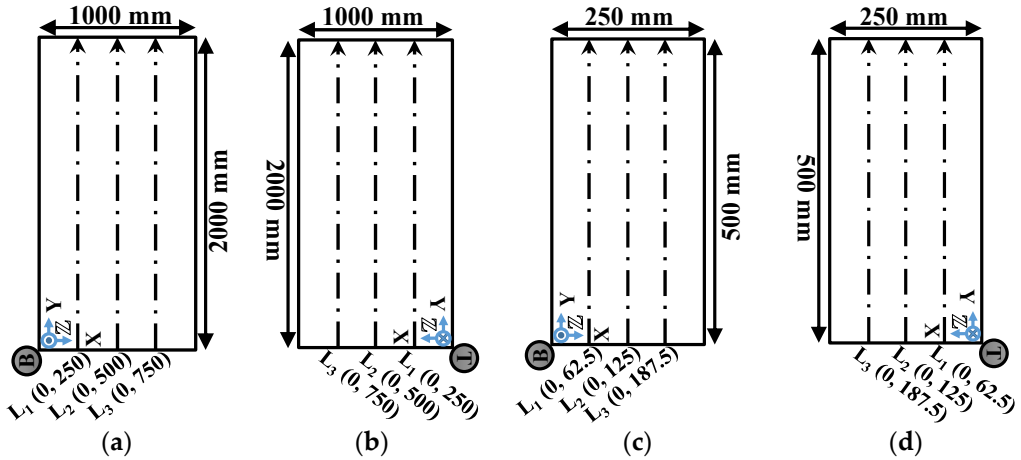

Figure 1. The measurement lines for acquiring the joint roughness coefficient (JRC) value for the fracture surfaces of the large (**a**,**b**) and medium (**c**,**d**) rock blocks. The viewing direction is toward the fracture surface, either bottom (B) or top (T) of the slab.

2.3.2. Roughness Measurements Using Photogrammetry

The rock fracture surfaces were scanned by taking a number of high-resolution photographs with two dip angles of 30° and 60° to reconstruct a 3D model of the fracture surfaces using the structure-from-motion photogrammetric method (Figure 2a). The camera was mounted on a camera slider, and the sample was placed in a fixed position (Figure 2b). A photographing procedure was developed to rationalize and simplify the process. This procedure consists of scanning the entire slab via the combination of several high-resolution images taken from two different tilt angles and in the positive/negative directions along X and Y axes. Each point on the slab is seen through this procedure at least eight times, in four different directions (positive and negative of X and Y directions) and from two different tilt angles (30 and 60 degrees). Two selected tilt angles are optimal to maximize point matching accuracy (Figure 2) [64].

The photogrammetry of different parts of the slab was conducted with different procedures. The origin corner was locked with 13 images taken manually in a circular motion with the camera pointing towards the corners (three-quarters of the corner's periphery) (Figure 3a). The blue arrows in Figure 3a illustrate the position and orientation of the camera at each of the 13 steps, as well as the direction followed. Each corner was photographed in the same way while moving along the edges. The corners were shot only once per angle for a total of 144 images (72 per angle). The sides of the slab were scanned by continuous image-taking along the sides. The camera lens was pointed inwards at a 45° angle from the edge being photographed. The path followed is represented in Figure 3a by the black dashed arrows and the numbers represent the sequence followed. The arrows show the position and orientation of the camera. Figure 3b, on the other hand, illustrates the backward direction (the purple dashed arrows) and the new position of the camera. After the perimeter had been photographed, the inner area of the slab was shot following similar steps as in the shooting of the edges. Defined paths were used to cover the central part of the slab while providing enough reference points by means of the sequence of the shooting, performing the same backward-and-forwards movement. Parallel to each axis, the lanes were spaced at every 25 cm for the large sample and at every 7.5 cm for the medium sample (Figure 3c,d).

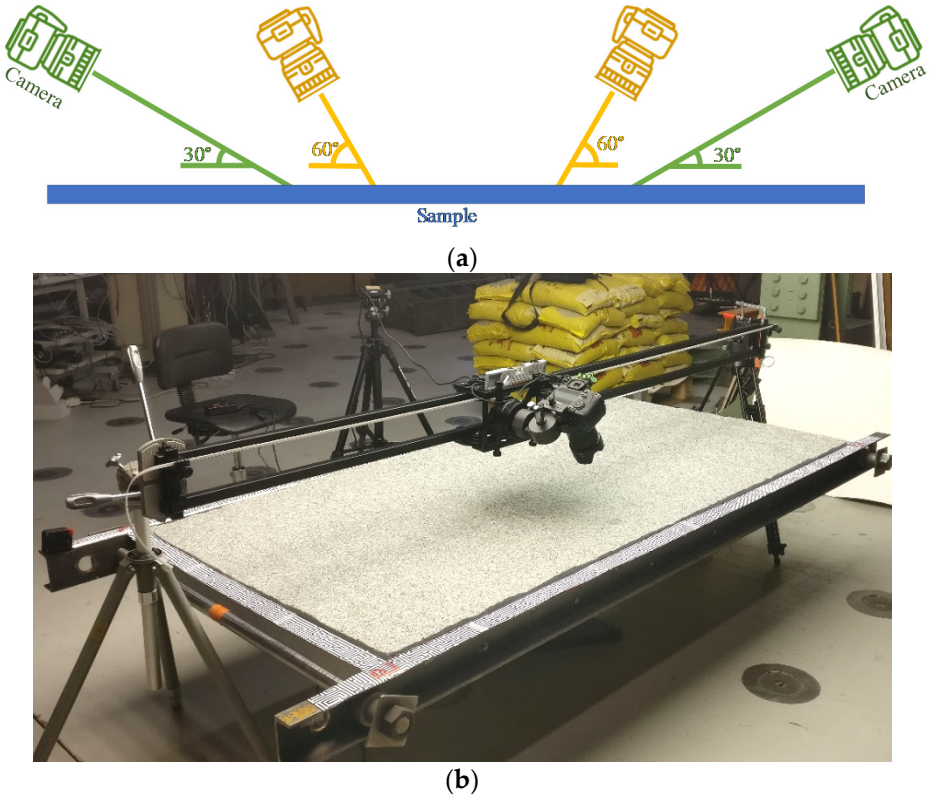

Figure 2. The photogrammetry setup with (**a**) camera positioning in the back-and-forth photographing direction, (**b**) the slider track setup.

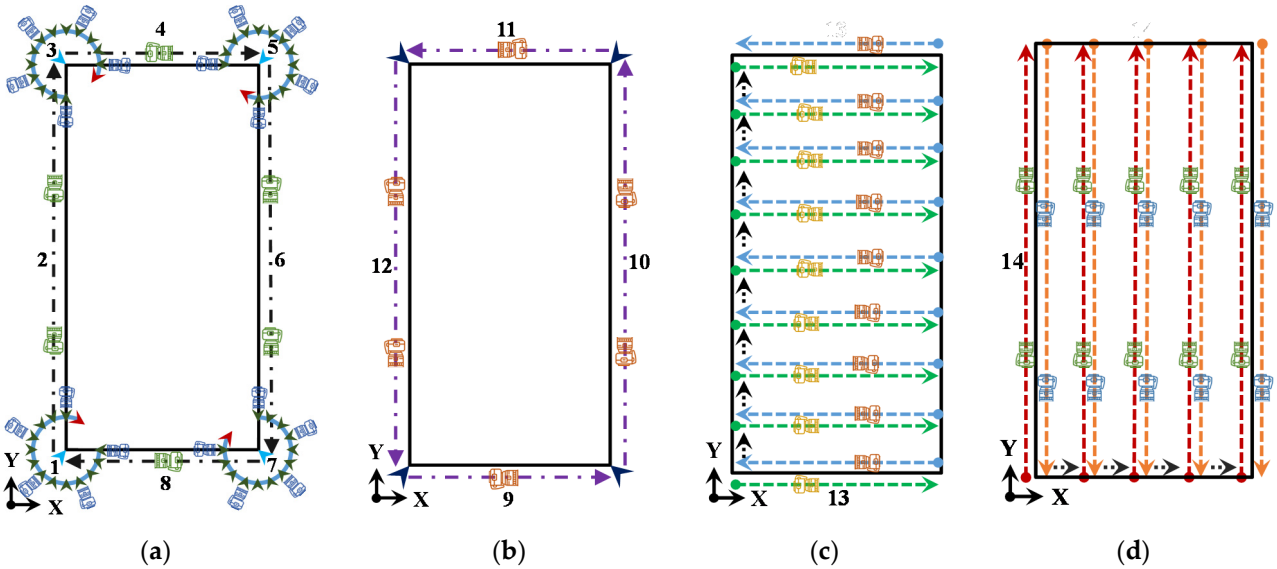

Figure 3. Diagram illustrates the camera movement to photograph the horizontal slab. (**a**) along corners and edges (**b**) opposite direction along the edges and the corners (**c**) shooting along the positive and negative X-axis and (**d**) along the positive and negative Y-axis.

The photographs were taken using a Canon 5DS R DSLR camera and a Canon 35 mm f/1.4L II USM lens. The ISO sensitivity was set to 400, and the aperture was set to f/11. The methodology used for the acquisition of the pictures follows the basic guidelines developed in the previous stages of the KARMO-Mechanical Properties of Rock Joints project [46,65]. The set of photos obtained from this process was used as the data input to generate point

clouds with the VisualSfM open-source software [66]. The point clouds obtained were then denoised and triangulated with the CloudCompare open-source software to create a mesh replicating the rocks' surfaces [67]. JRC values and damaged areas can be determined by the evaluation of the topographies of the fractures.

The comparison between the pre-test and post-test surface point clouds was conducted in CloudCompare. It can help identify the areas on the sample surfaces that experienced the most damage during the mated stages of the shear tests. For each slab, pre-test and post-test point clouds were imported into CloudCompare. The pre-test cloud was used as a reference cloud for this step, and the post-test cloud was aligned to it. Next cloud-to-cloud absolute distance was calculated as a scalar field. As it is an absolute distance, the software does not indicate whether the deviation is positive, indicating a gap or negative, indicating an alignment error where the sample occupies the same volume.

2.4. Photogrammetric Joint Roughness Coefficient (JRC) Calculation from a 2D Line

To evaluate the joint roughness coefficient (JRC) in the photogrammetry method, statistical solutions were used, giving an estimate of the roughness amplitude and surface texture. To accomplish this objective, 2D cross-sectional lines were extracted by drawing them on the point clouds, similarly to the lines in Figure 1. In this study, root mean square (RMS) characterization of local slopes [18] and modified root mean square [21] were applied to assess the roughness. The slope measurement proposed in [18] is the RMS estimate from the local slopes of the profile with intervals between measured data points. The relationship with JRC and RMS can be represented thus (Equation (2)):

$$JRC = 32.2 + 32.47 \log (Z_2), \tag{2}$$

where Z_2 represents the RMS (Equation (3)):

$$Z_2 = \sqrt{\frac{\sum_i^{N-1}(z_i - z_{i+1})^2}{(N-1)ds^2}}, \tag{3}$$

where z is the height of the profile above the line, N the number of measurements, and ds the incremental width in horizontal direction. The two-dimensional sectioning profiles were normalized with a sampling interval of 0.5 mm to maintain optimal behavior of the statistical JRC modelling, as this interval was originally used for the distance between measurements (ds). The mean inclination angle of fracture asperities was merely taken into account in this method. Neglecting the scale effect and the influence of amplitudes are drawbacks of this method. To overcome these disadvantages, a general logistic function is formulated as Equation (4) [21]:

$$JRC = \frac{40}{1 + e^{-b\lambda}} - 20, \tag{4}$$

where b represents a constant value when it equals 20 for suggested JRC values and λ signifies a roughness index obtained from Equation (5):

$$\lambda = \left(\frac{h}{L}\right)^{1/3} (Z_2')^{2/3}, \tag{5}$$

where h is the mean height of the surface asperities, defined by Equation (6):

$$h = \frac{1}{L}\int_{x=0}^{x=L} |z| dx = \sum_{i=1}^{N} \frac{|z_{i+1} + z_i|(x_{i+1} - x_i)}{2L}, \tag{6}$$

where L is the length of the profile, x_i and z_i are the x-coordinate and the z-coordinate points along the profile, respectively, and Z_2' denotes the Modified Root Mean Square written as Equation (7):

$$Z_2' = \sqrt{\frac{1}{L}\int_{x=0}^{x=L}\left(\max\left(0, \frac{dz}{dx}\right)\right)^2 dx} = \sqrt{\frac{\sum_{i=1}^{N}(max(0, z_{i+1} - z_i))^2}{(x_{i+1} - x_i)L}}, \quad (7)$$

The average of the JRC values of the lines was used to determine the JRC value of each surface.

2.5. Push-Shear Test Setup

The method selected to obtain the peak and residual shear strengths of the samples was a multi-stage shear test consisting of pushing the top rock slab over the rough surface of its fixed counterpart, according to the recommendations of the ISRM revised method for determining the shear strength of rock fractures in the laboratory [68]. All the stages, their descriptions, and the normal stresses for the large and medium samples are presented in Table 1.

Table 1. Shear test stages and loads used in the large sample shear test.

Phase	Description	Normal Stress (kPa)
Pre-test	Photogrammetry	
First stage:	Pushing without extra normal stress	3.6
Damage mapping 1	Visual assessment of damage locations and resetting	
Second stage:	Pushing with extra normal weight	6.0
Damage mapping 2	Visual assessment of damage locations and resetting	
Third stage:	Pushing with extra normal weight	8.5
Damage mapping 3	Visual assessment of damage locations and resetting	
Fourth stage:	Pushing without extra normal stress	3.6
Damage mapping 4	Photogrammetry	
Fifth stage: Unmatched residual	Pushing without extra normal stress, top sample rotated through 180°	3.4

Two shearing rates were used, 0.1 mm/min until peak shear strength, followed by a shearing rate of 0.5 mm/min until the moving half had been displaced by 2.5% (50 mm) of the length of the large sample (2000 mm) and 10% (50 mm) of the length of the medium sample (500 mm). Because of the large size of the rock samples, hydraulic cylinders to apply normal stress were ruled out. The displacement of the rock slab would have inclined the cylinders, causing changes in the angle of the applied pressure. Instead, a dead weight pressure was used on top of the slab to maintain the normal component (Table 2). Each bag was weighed and labeled with its actual weight. As a result, the normal stresses used for the shearing test are low compared to in situ rock conditions.

Table 2. Weight and normal stresses used in the large and medium tests.

Phase of Shearing Test	Weight (kg)							Normal Stress (kPa)
	Large Sample Test				Medium Sample Test			
	Slab	Frame	Additional	Total	Slab	Additional	Total	
First stage	697.60	34.5	0	732.10	17.11	28.65	45.76	3.6
Second stage	697.60	34.5	500.23	1232.33	17.11	59.91	77.02	6.0
Third stage	697.60	34.5	1000.20	1732.30	17.11	91.16	108.27	8.5
Fourth stage	697.60	34.5	0	732.10	17.11	28.65	45.76	3.6
Fifth stage	697.60	0	0	697.60	17.11	26.49	43.60	3.4

Figure 4 illustrates the test setup before shearing the sample. The top slab rests on the bottom slab with freedom of movement in the horizontal direction, i.e., along the shearing direction, Y-axis. For the large sample, a couple of 2.5 m steel beams are screwed onto the sides of the slab to handle it. Additional shorter steel beams are attached below the steel bars to prevent the rotation of the top slab as a result of the uneven sliding surface. These shorter beams make contact with the bottom slab through four ball-bearing plates to allow horizontal movement and reduce the friction between the elements. U-shaped steel beams with UNP100 profile are used to transmit the load and those below the frame to restrain rotation. The weight of the steel elements is considered as part of the normal stress. In the fifth stage of the shearing test, the frame was removed from the large slab. To have same amounts of normal stress for the large and medium samples, the additional weight for the medium sample was reduced.

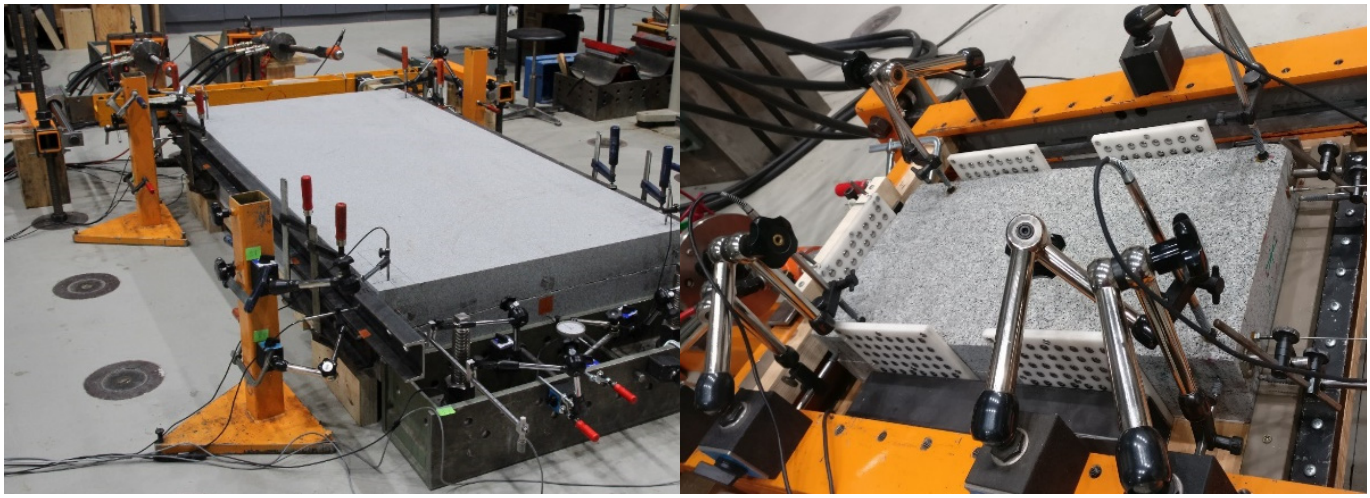

(**a**) (**b**)

Figure 4. Push shear test setup for the large sample: large sample 2000 mm × 1000 mm (**a**), and medium sample 500 mm × 250 mm (**b**).

The bottom slab rests on a wooden pallet that provides the necessary height to locate the centroid of the top slab at the same elevation as the cylinders. A steel block serves as a barrier to the bottom slab, restricting its movement. The barrier is fixed in place by two heavy-duty floor anchors.

The shearing force is applied by a pair of hydraulic cylinders parallel to the surface of the fracture and the direction of pushing is considered horizontal and transmitted to the top sample through a perpendicular steel beam with an H-shaped cross-section (HEM or H-beam) and a couple of wooden blocks fastened to the steel beams of the frame. A coupling system composed of a pair of steel plates and a ball-bearing plate is used as a connection point between the H-beam and the wooden blocks. The H-beam is restrained in its lateral movement by a pair of ball bearing plates allowing movement along the Z-axis (pushing direction) and Y-axis (vertical direction). Two HSS sections keep the guide cylinders in position. The pushing cylinders connect with the H-beam through a pair of wooden plates to center the cylinders and keep them in place while the force is applied (Figure 5 and Appendix A).

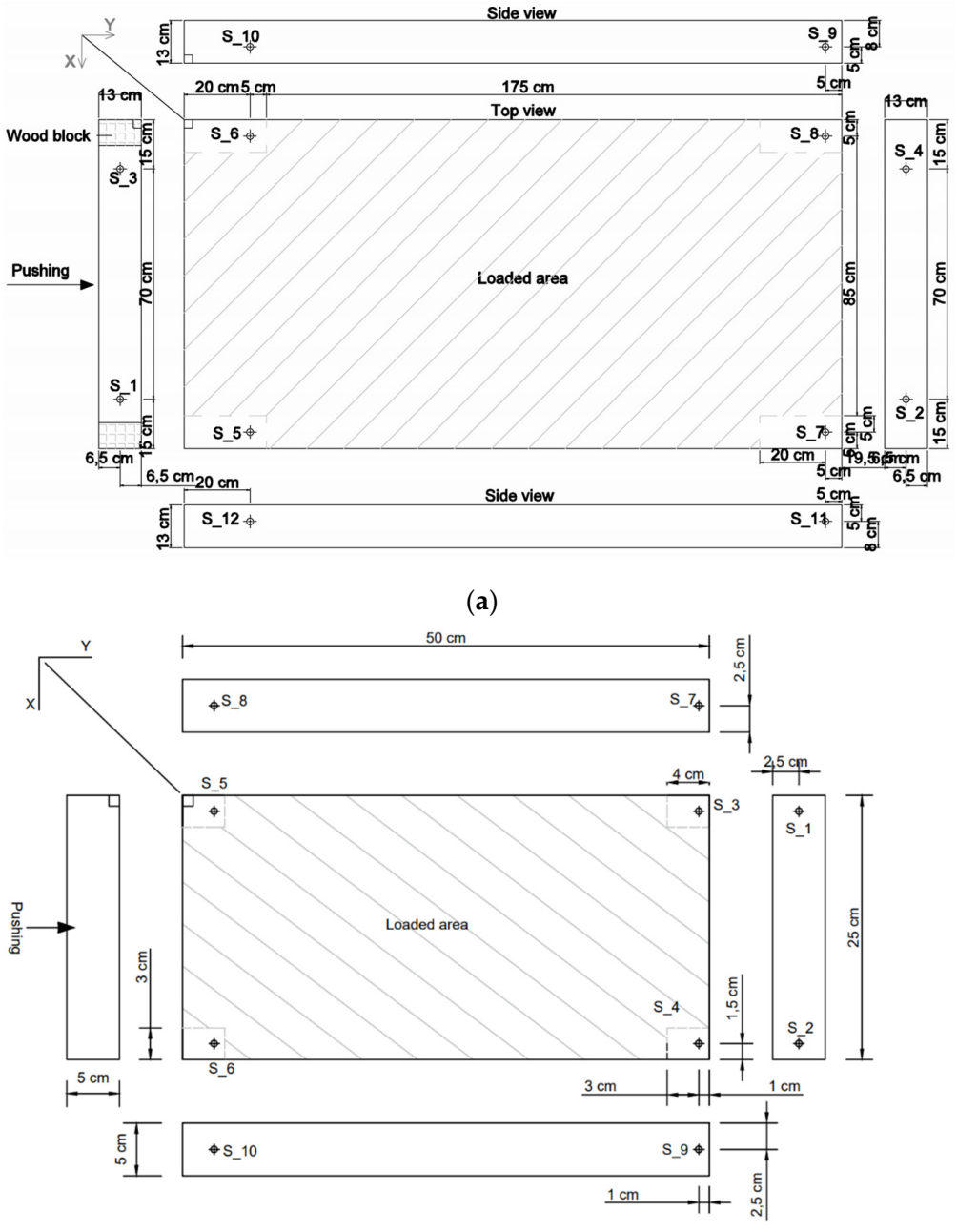

Figure 5. Layout of the locations of the displacement sensors: (**a**) large, and (**b**) medium. The positions of the linear variable differential transformers (LVDTs) are shown by the symbol S.

The displacement in all directions (x-, y-, and z-) is tracked with 12 and 11 linear variable differential transformers (LVDTs) in the large and medium samples, respectively (Figure 5). Additionally, each piston has a force sensor and an LDVT that measures the longitudinal displacement of the cylinder, and it is also used to measure the shearing displacement rate.

2.6. Estimation of Peak Friction Angle

An empirical equation (Equation (8)) was developed by Barton [15] to estimate the peak friction angle (φ_p) as follows:

$$\varphi_p = \varphi_b + JRC \log(JCS/\sigma_n), \quad (8)$$

where φ_b is the basic friction angle, JCS is the joint compressive strength, σ_n is the normal stress on the failure plane, and JRC is the joint roughness coefficient. For the Kuru granite, φ_b was measured with the tilt table test as 33° [47], for JCS the UCS of 216 MPa was used, and σ_n is according to Table 2. The JRC values were estimated by the aforementioned methods: the profilometer and statistical methods. The calculated values of the peak friction angle obtained in this way were compared to the values obtained from the back-calculation of the direct shear test results with Equation (9) developed by Bandis et al. [5]:

$$\tau = \sigma_n \tan(\phi_r + JRC \log(JCS/\sigma_n)) = \sigma_n tan(\phi_p), \quad (9)$$

where τ is the peak shear strength of the rock joints.

3. Results and Discussions

3.1. Characterization of Damaged Areas of the Fracture Surface

Figure 6 shows the mapped damage of the bottom surface. The damage was evident after every shearing stage.

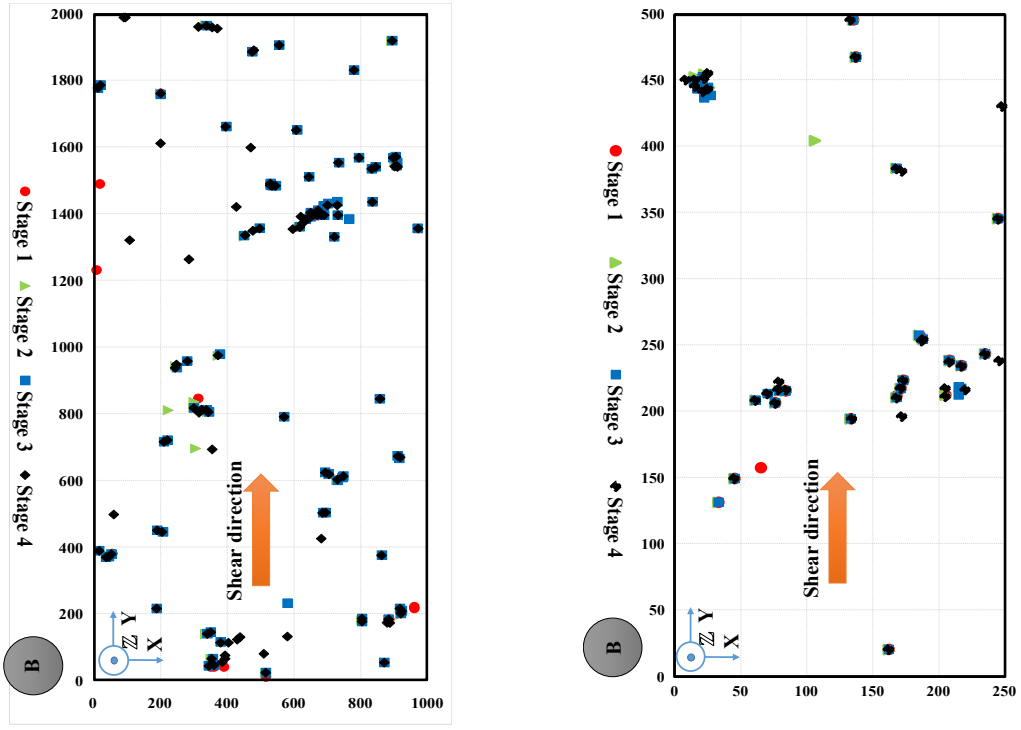

(**a**) (**b**)

Figure 6. Damage mapping after four shearing stages on the bottom surface of the sample mapped by a ruler: (**a**) large sample and (**b**) medium sample. The colored dots show damaged areas in the different stages of the shear tests.

The photogrammetry data provide an opportunity to detect and inspect fracture surfaces in detail. The initial and the sheared surfaces are illustrated in Figures 7 and 8. By comparing the topography of a fracture surface before and after the shearing test. As detected by the photogrammetry method, damaged areas are highlighted, and the damaged areas are spread almost all over the fracture surfaces.

3.1.1. JRC Estimated by the Profilometer

The visual comparison method was adopted for evaluating the JRC values of the fracture surfaces with the profilometer. Each line in Figure 1 was divided into 10 cm sections and the profilometer was positioned over each section. JRC values were estimated for each section by comparing the measured profiles with the 10 standard profiles. Figure 9 shows the manually defined JRC results for the rock slab surfaces before the shear tests. These values were averaged by Equation (1) to approximate the final JRC for each line, each fracture surface, and finally for both surfaces. The highly unequal distribution of JRC values for the large sample (Figure 9a) is obvious, ranging from 0–2 to 18–20. Visual inspection is always prone to bias. The JRC values were mapped independently for top and bottom surfaces and the length averaged measurements are almost identical for both the large and medium samples.

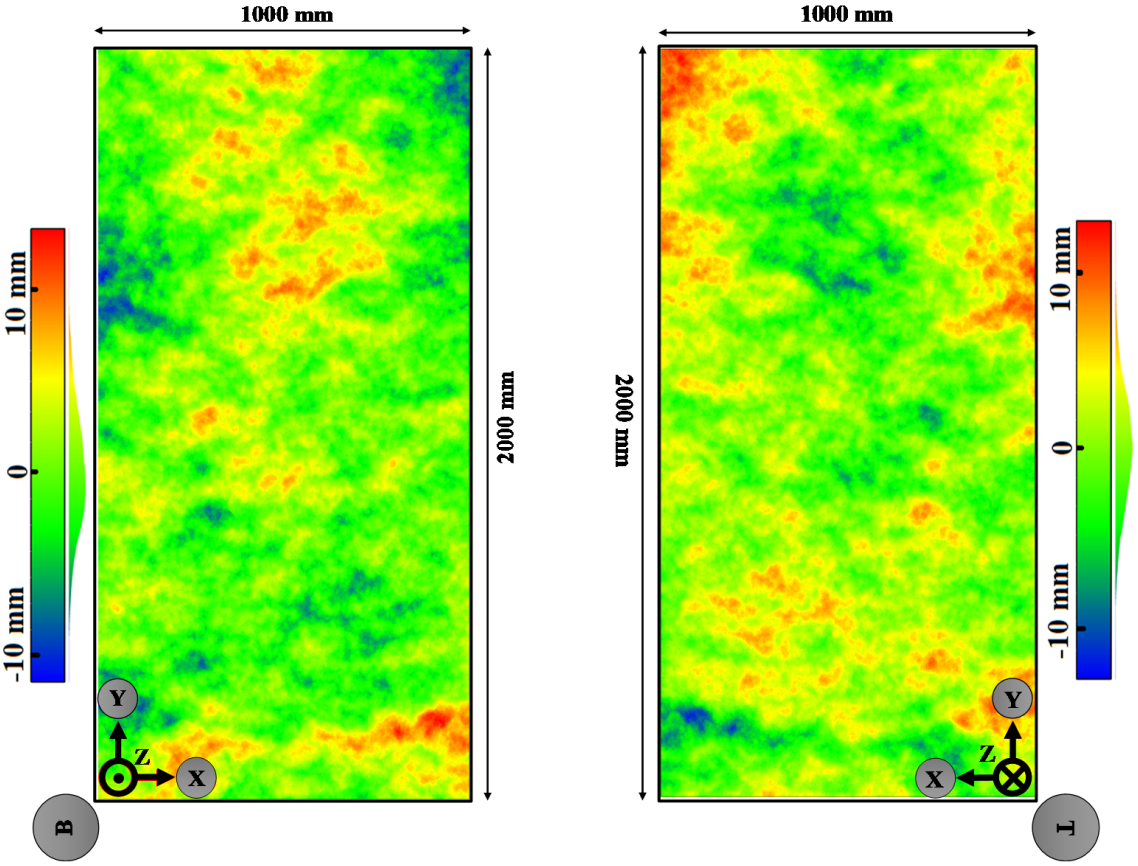

(**a**) Initial topography, bottom block to left and top block to right.

Figure 7. *Cont.*

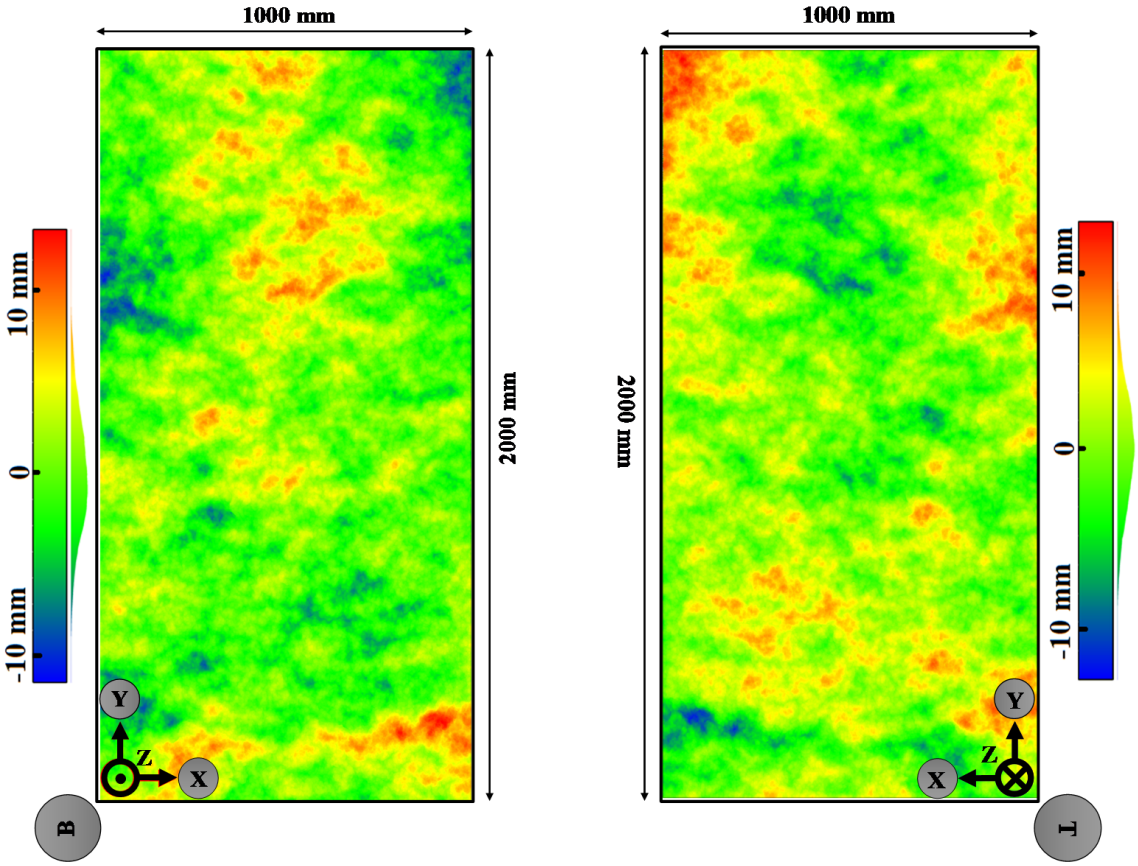

(**b**) Sheared topography, bottom block to left and top block to right.

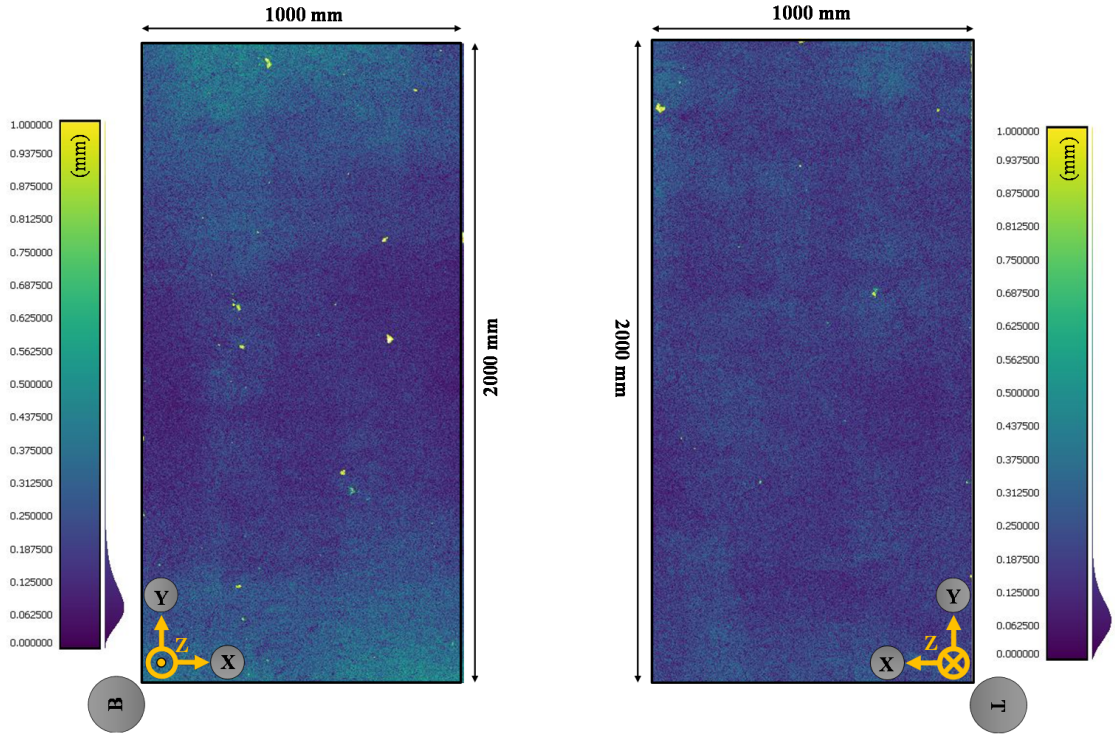

(**c**) Damaged areas based on the comparison between pre-shearing and post-shearing stages

Figure 7. Photogrammetry data of the large sample (2000 mm × 1000 mm), (**a**) initial topography, (**b**) sheared topography and (**c**) damaged areas based on the comparison between pre-shearing and post-shearing stages.

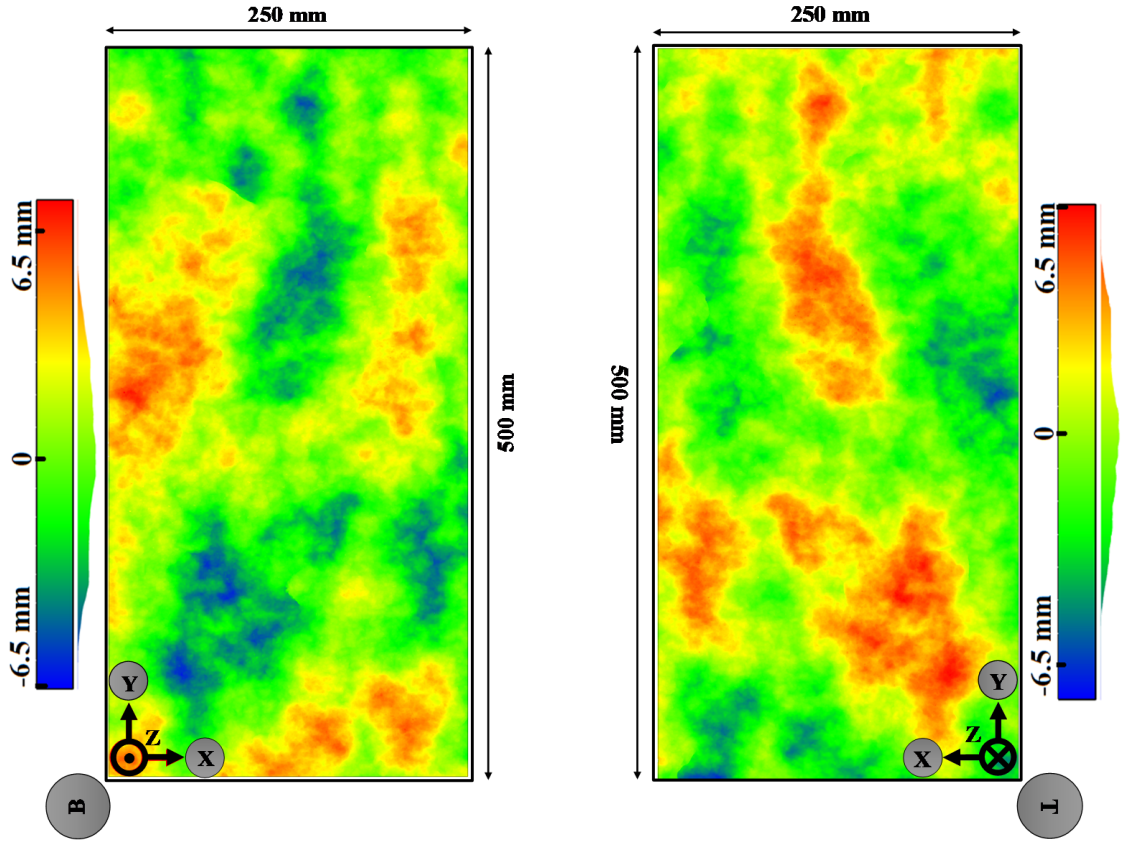

(**a**) Initial topography, bottom block to left and top block to right.

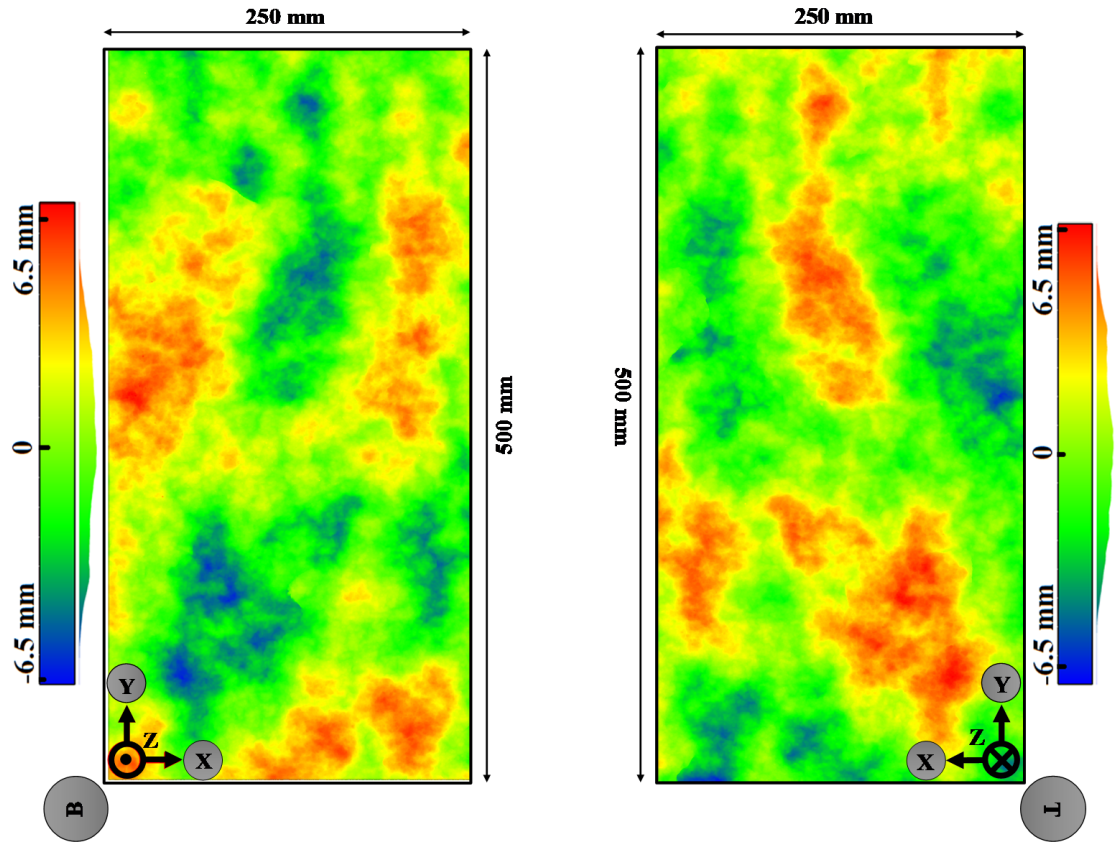

(**b**) Sheared topography, bottom block to left and top block to right.

Figure 8. *Cont.*

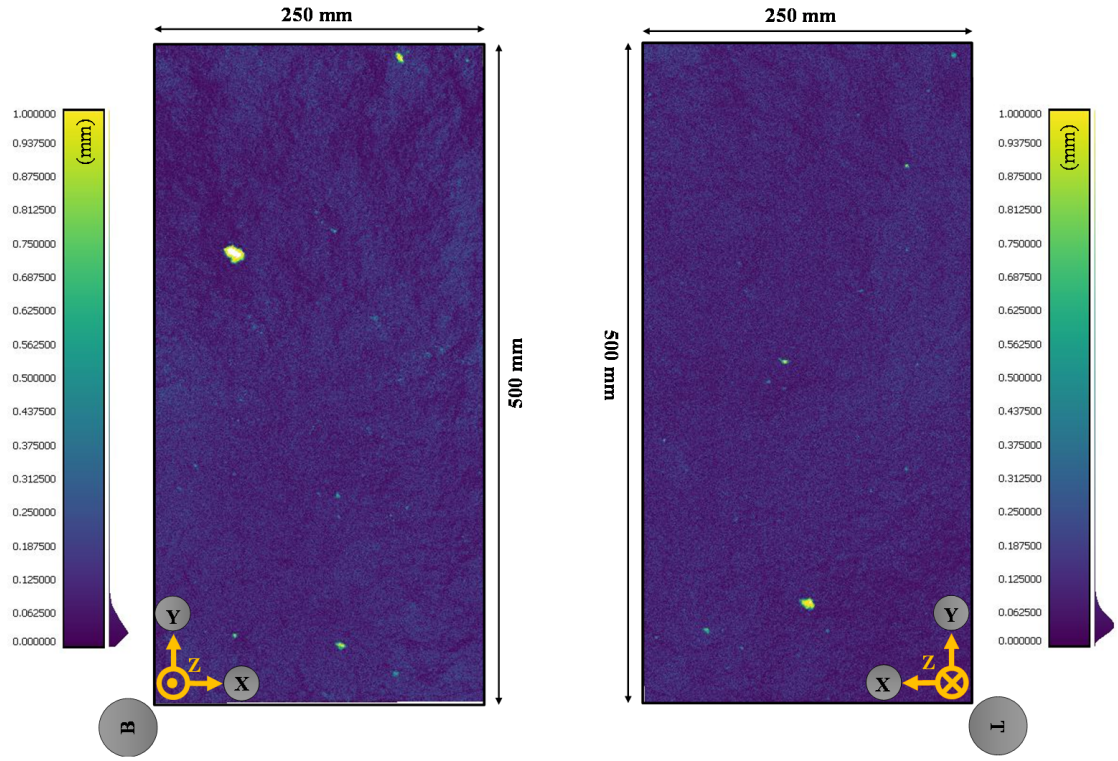

(**c**) Damaged areas based on the comparison between pre-shearing and post-shearing stages.

Figure 8. Photogrammetry data of the medium sample (500 mm × 250 mm), (**a**) initial topography, (**b**) sheared topography and (**c**) damaged areas based on the comparison between pre-shearing and post-shearing stages.

3.1.2. Photogrammetric JRC Values

The 2D cross-sectional YZ coordinates of each profile were extracted from the photogrammetric models. The JRC values were estimated for the divided 10 cm profiles, similarly to the profilometer method. The JRC values were then calculated for each section using Equation (2) (Figure 10). The distribution of the JRC values is between 6–8 for the large sample and 12–14 for the medium sample.

To consider the effect of scale on the JRC values, Equations (4) to (7) were employed with the extracted photogrammetric data. The calculated JRC values are shown in Figure 11. A comparison among the JRC, Z'_2, Z_2 methods shown in Table 5 reveals that the modified RMS (Z'_2) resulted in significantly lower JRC values for the large sample from approximately 10 to approximately 7 (Figures 9a, 10a and 11a). There is no remarkable difference between the JRC from the profilometer (9.3) and Z'_2 (8.9) methods for the medium sample. However, the JRC values obtained from Z_2 (10.9), or the medium sample, are greater by almost 2 JRC units or 17% of the JRC value.

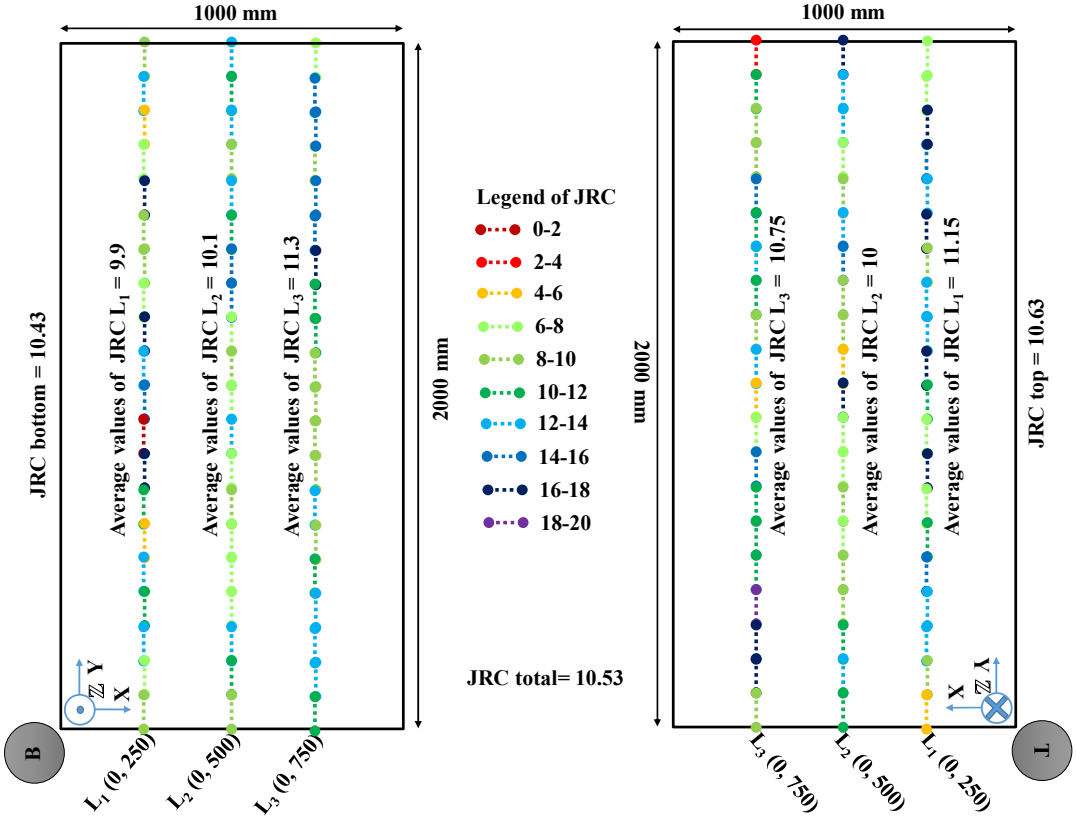

(**a**) JRC before shearing of the large sample

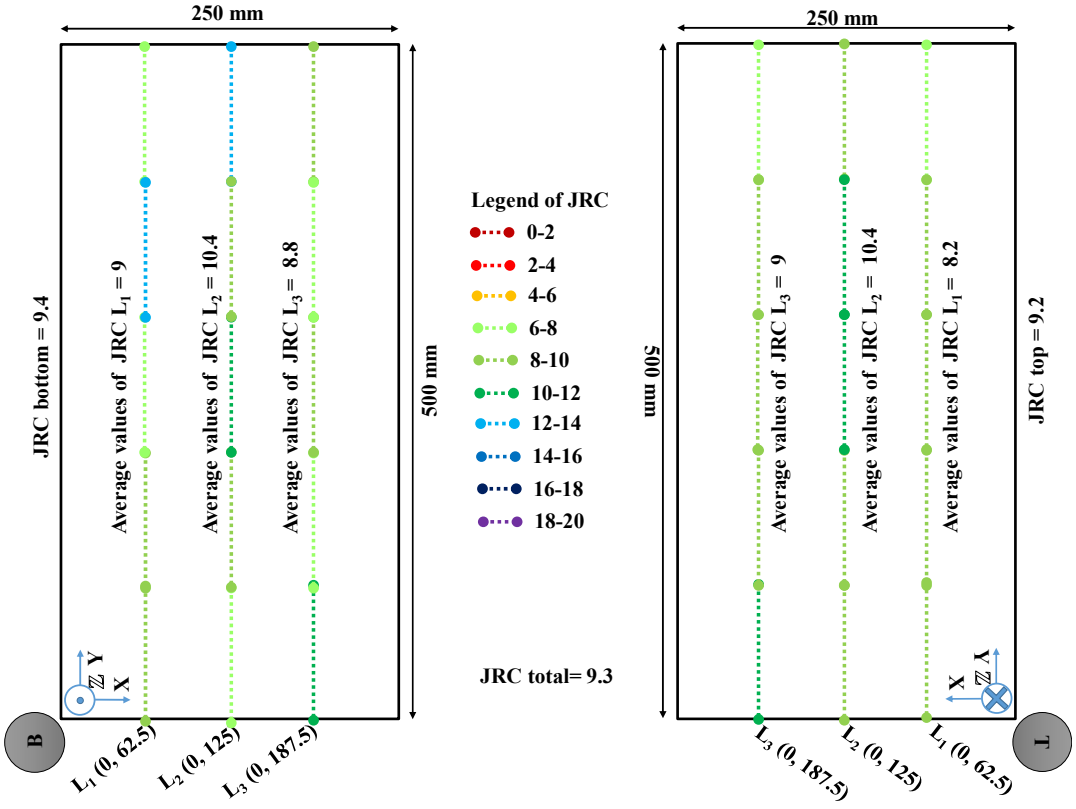

(**b**) JRC before shearing of the medium sample

Figure 9. The JRC profilometer results of the slabs; pre-shearing of the large sample (**a**), pre-shearing of the medium sample (**b**).

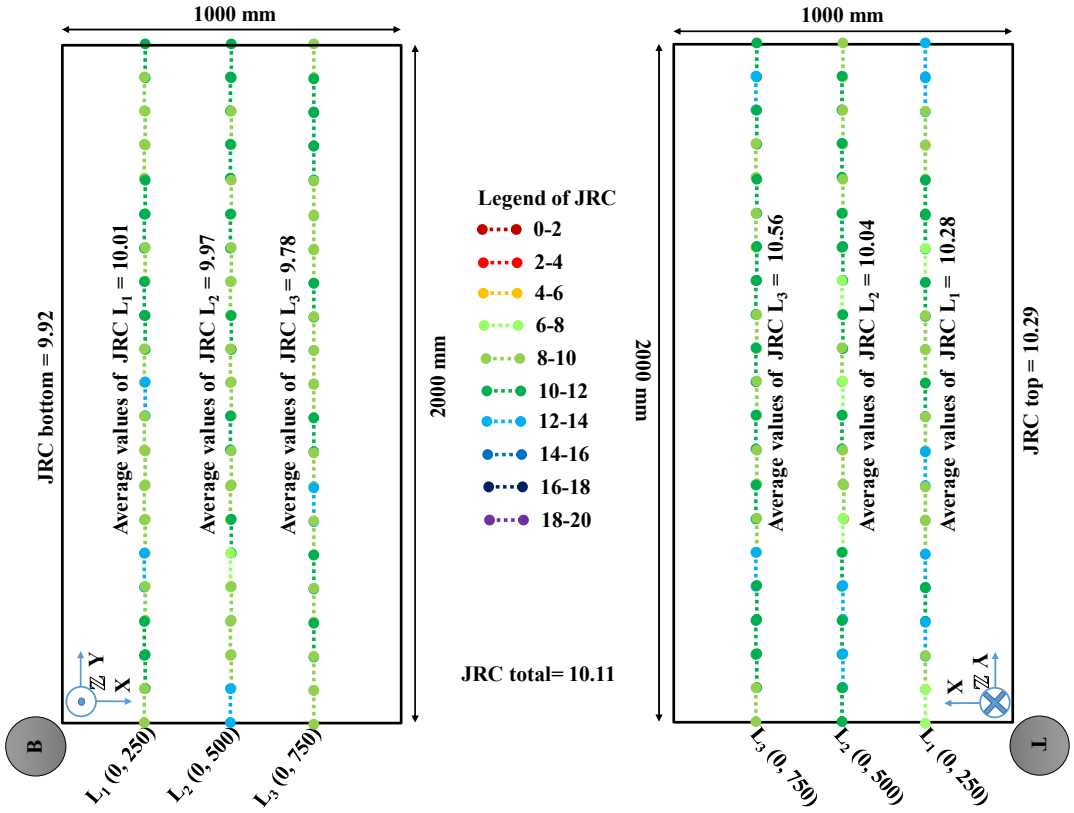

(**a**) Before shearing of the large sample

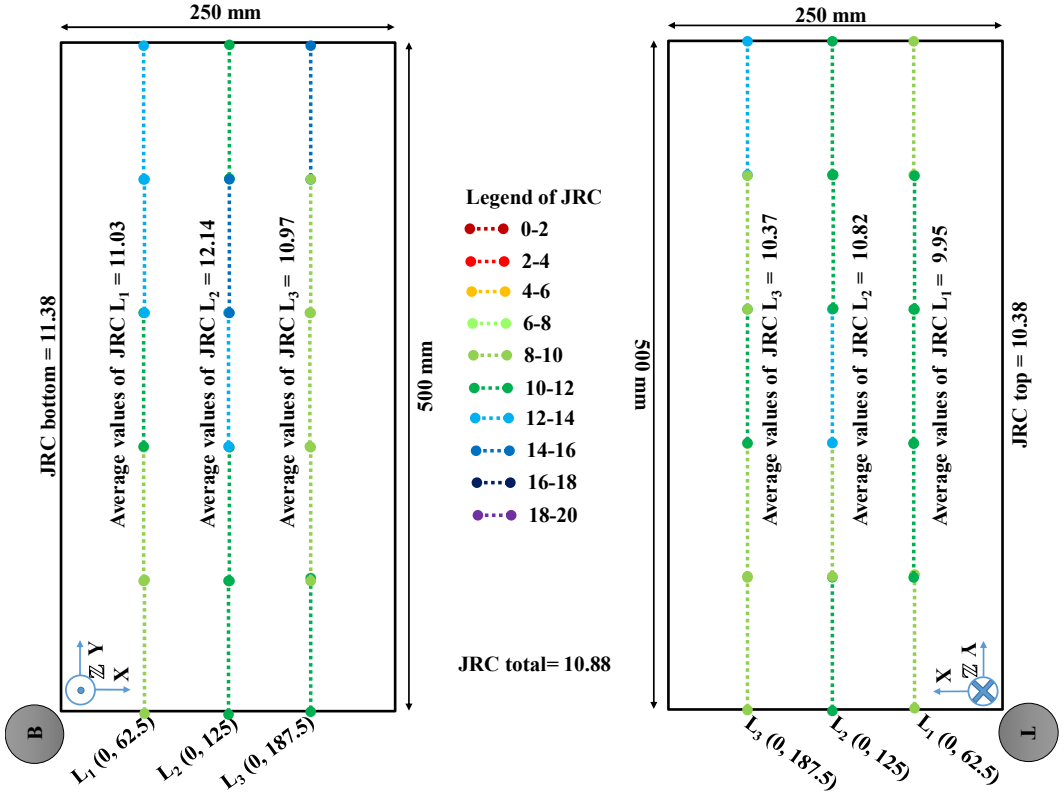

(**b**) Before shearing of the medium sample

Figure 10. The photogrammetry method and Z_2 to define the JRC roughness profiles of the slabs before shearing of the large sample (**a**), before shearing of the medium sample (**b**).

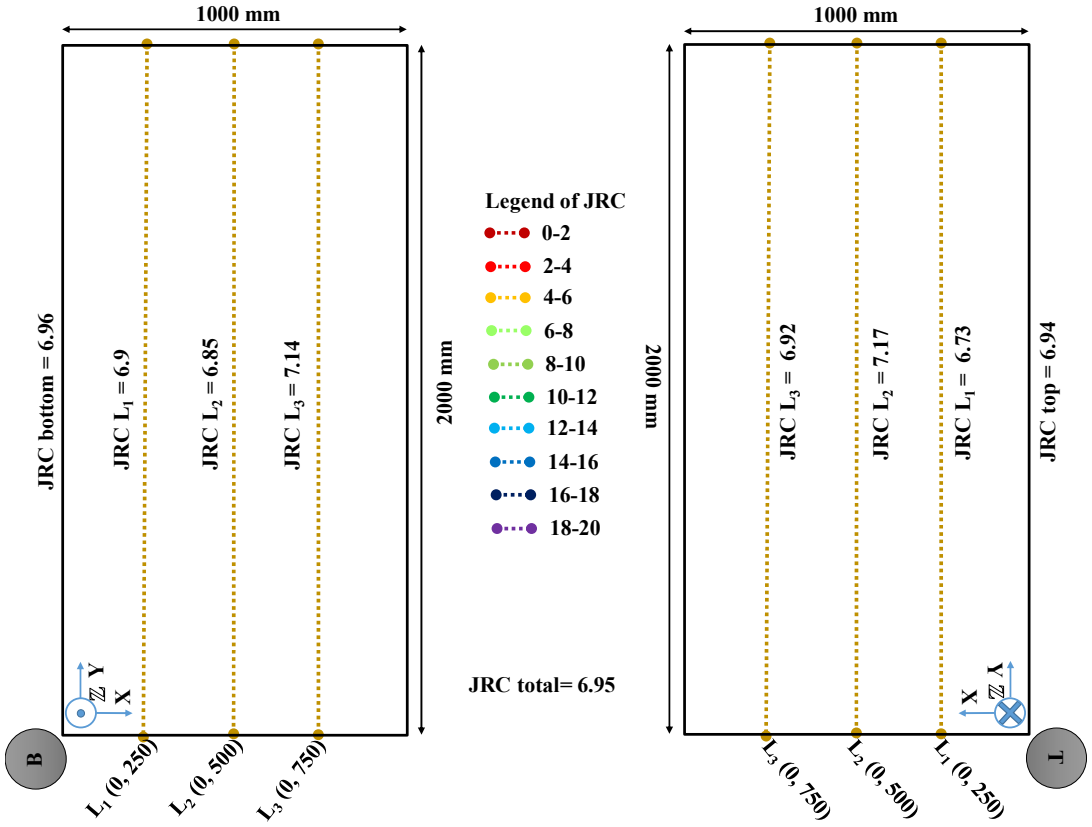

(**a**) Pre-shearing of the large sample (2000 mm × 1000 mm)

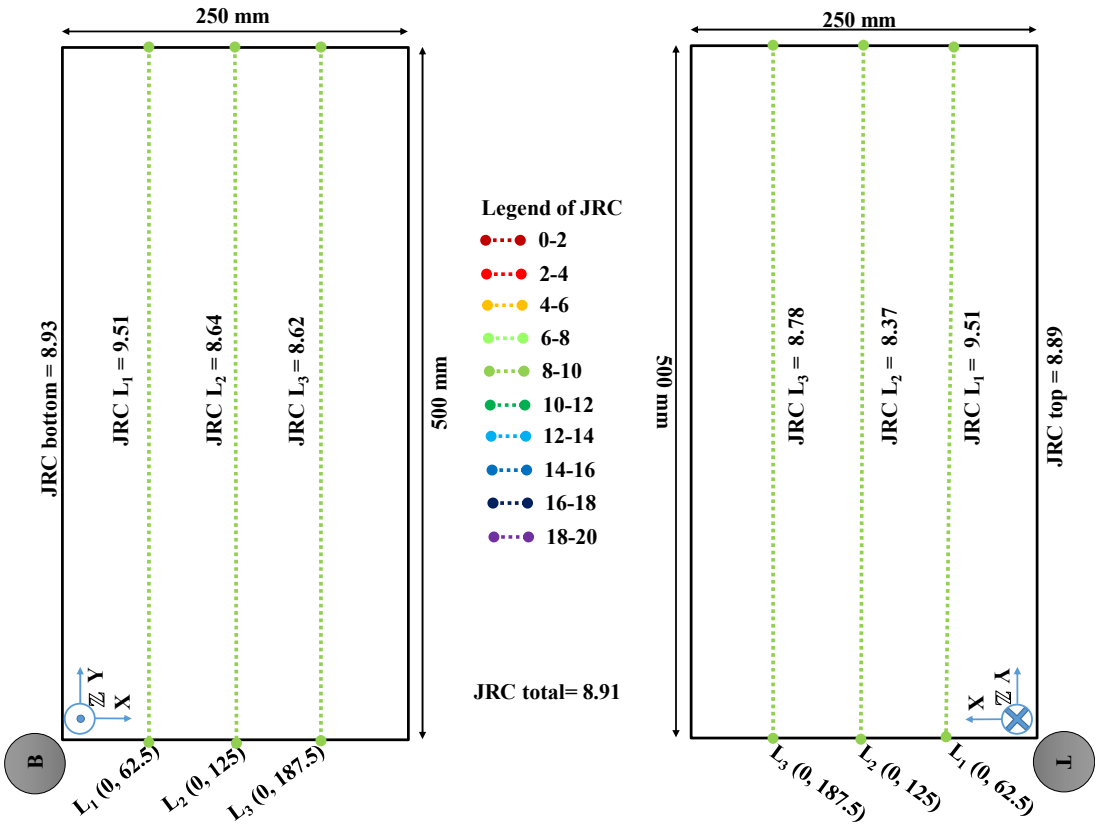

(**b**) Pre-shearing of the medium sample (500 mm × 250 mm)

Figure 11. The photogrammetry method and $Z'2$ to define the JRC roughness of the slabs (**a**) pre-shearing of the large sample (2000 mm × 1000 mm), (**b**) pre-shearing of the medium sample (500 mm × 250 mm).

3.2. Shear Test Diagrams

Figures 12–18 depict the results for shearing tests. The same methodology was used in both cases. Figure 12a shows the shear results of the large sample for the five stages of shearing (Tables 1 and 2). Figure 12b depicts the shear strengths before the peaks (Table 3).

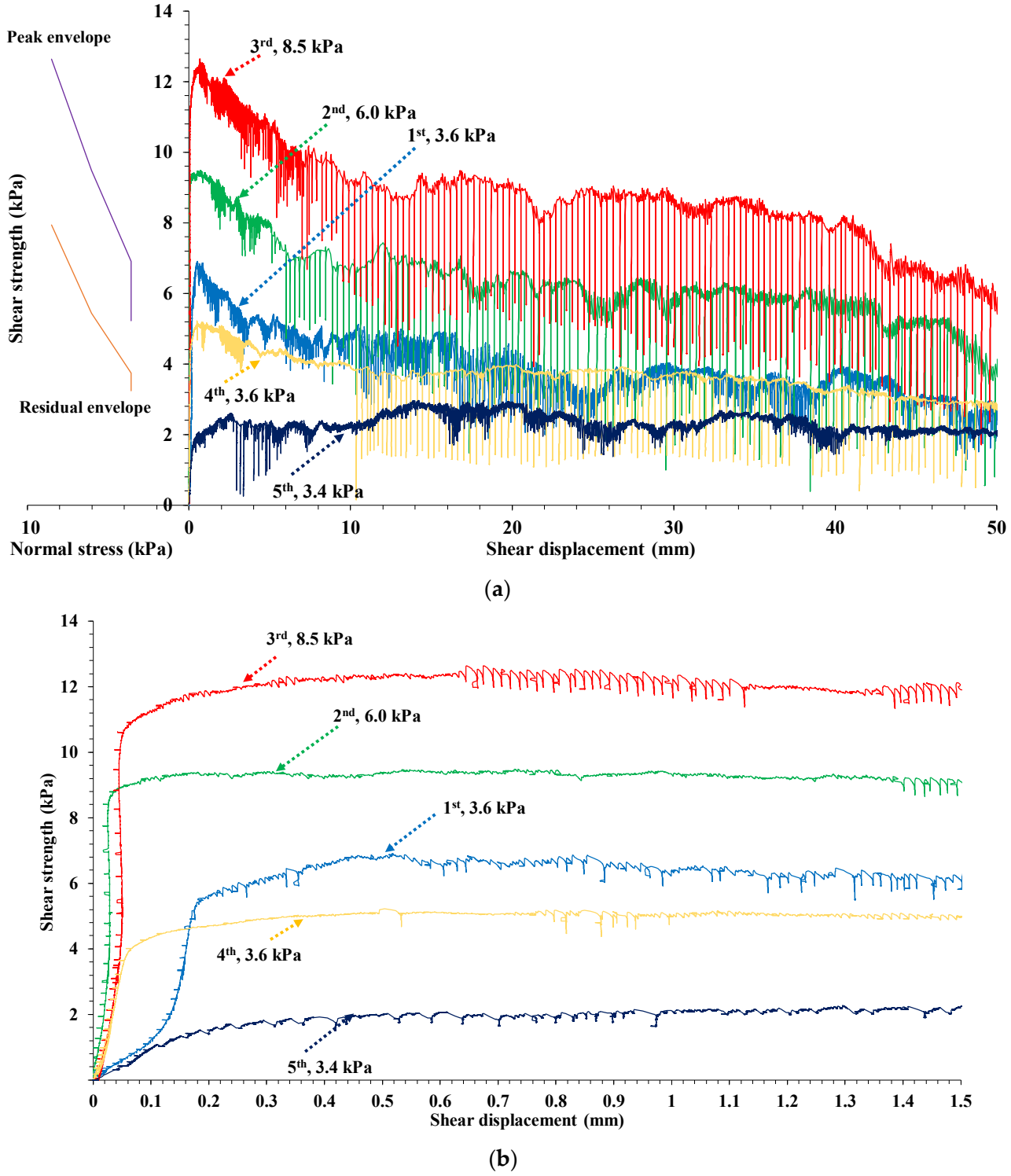

Figure 12. Shear test results for the large sample (2000 mm × 1000 mm) as a function of normal stress and shear displacement: (**a**) 50 mm displacement, (**b**) 1.5 mm displacement.

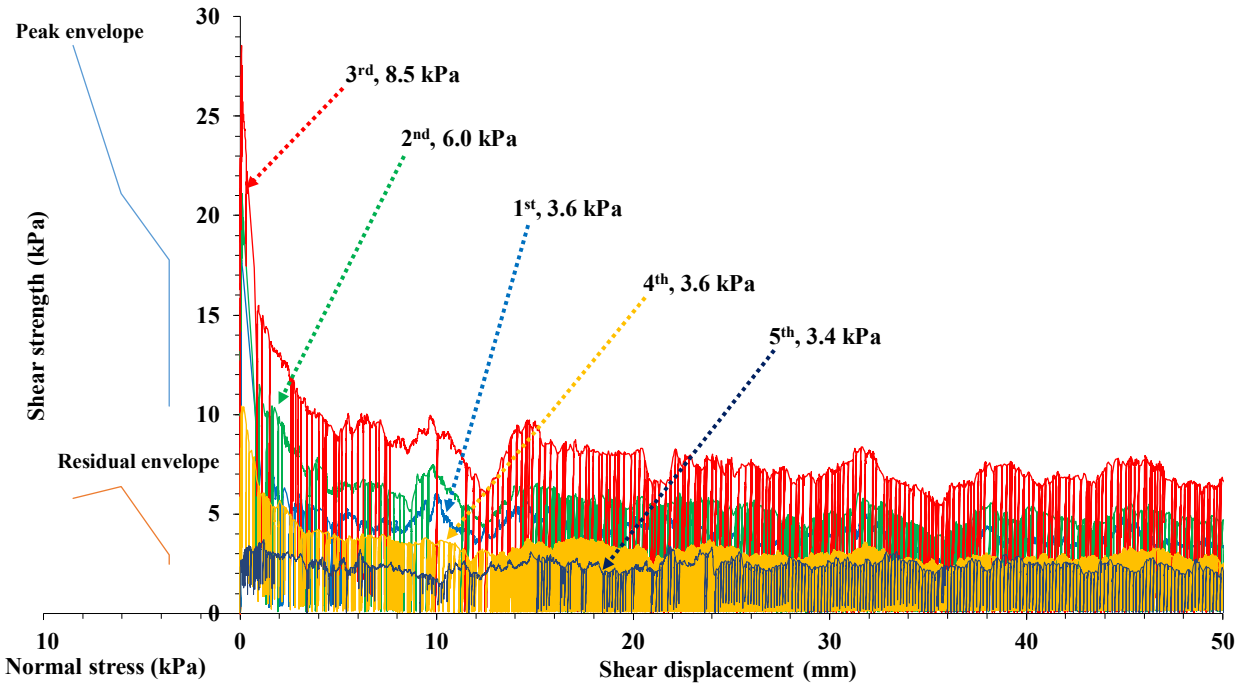

(**a**)

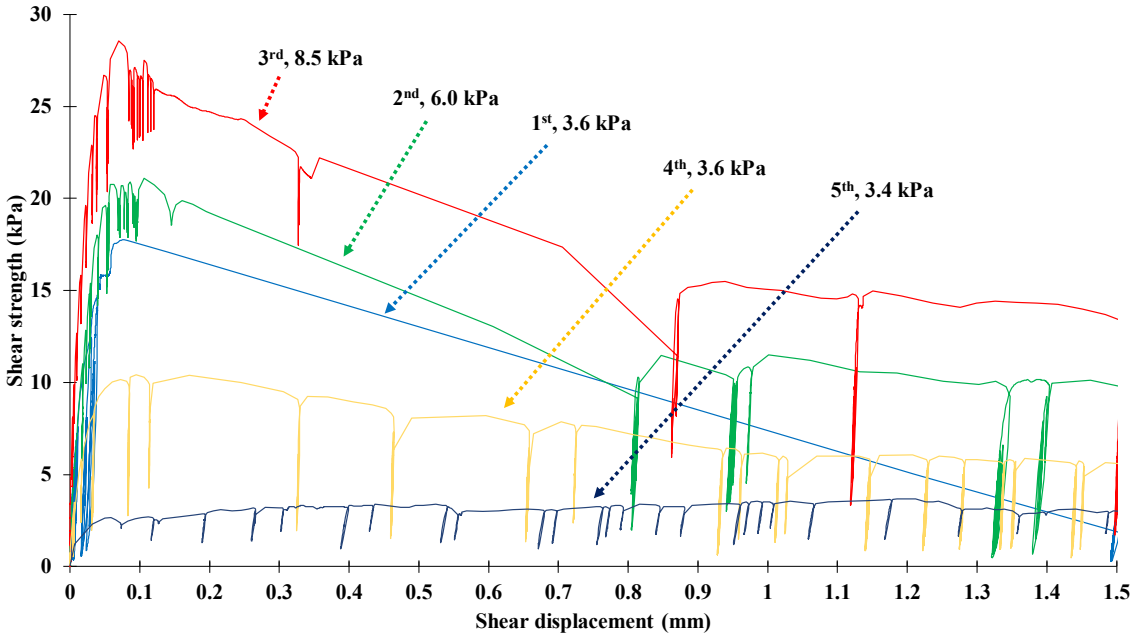

(**b**)

Figure 13. Shear test results for the medium sample (500 mm × 250 mm) as a function of normal stress and shear displacement: (**a**) 50 mm displacement, (**b**) 1.5 mm displacement.

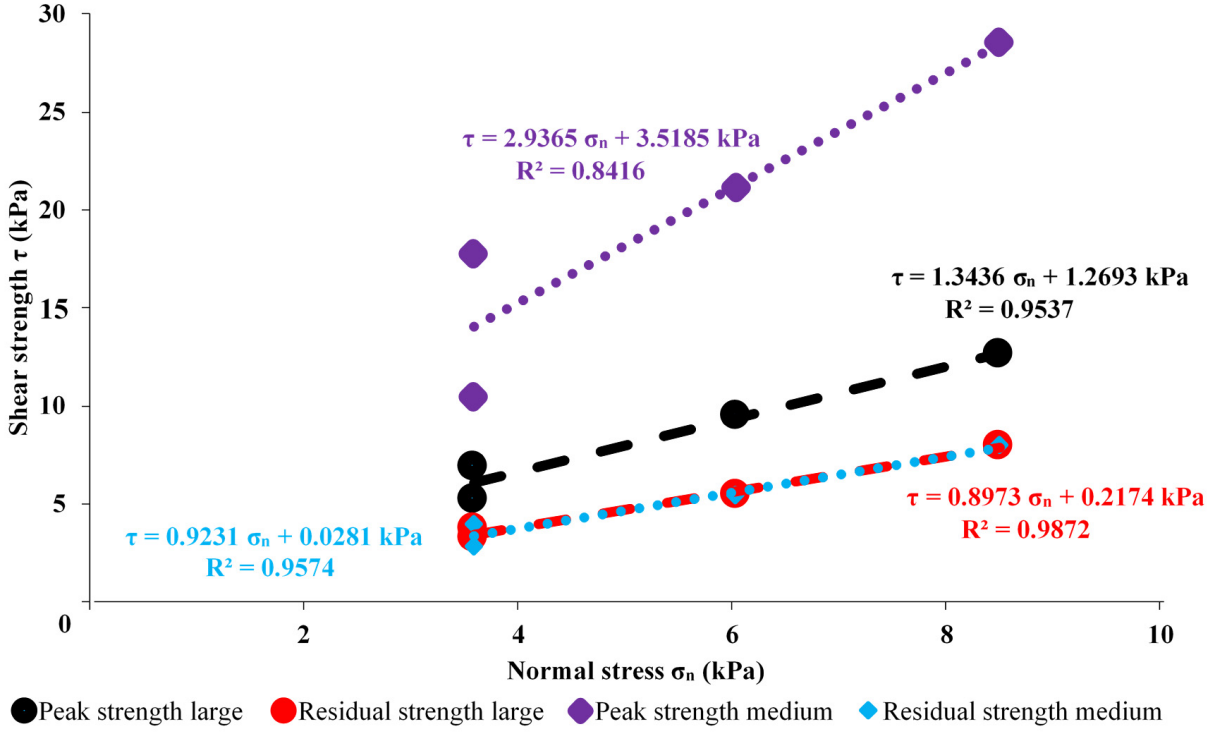

Figure 14. Peak and residual strength comparison for each stage at different scales.

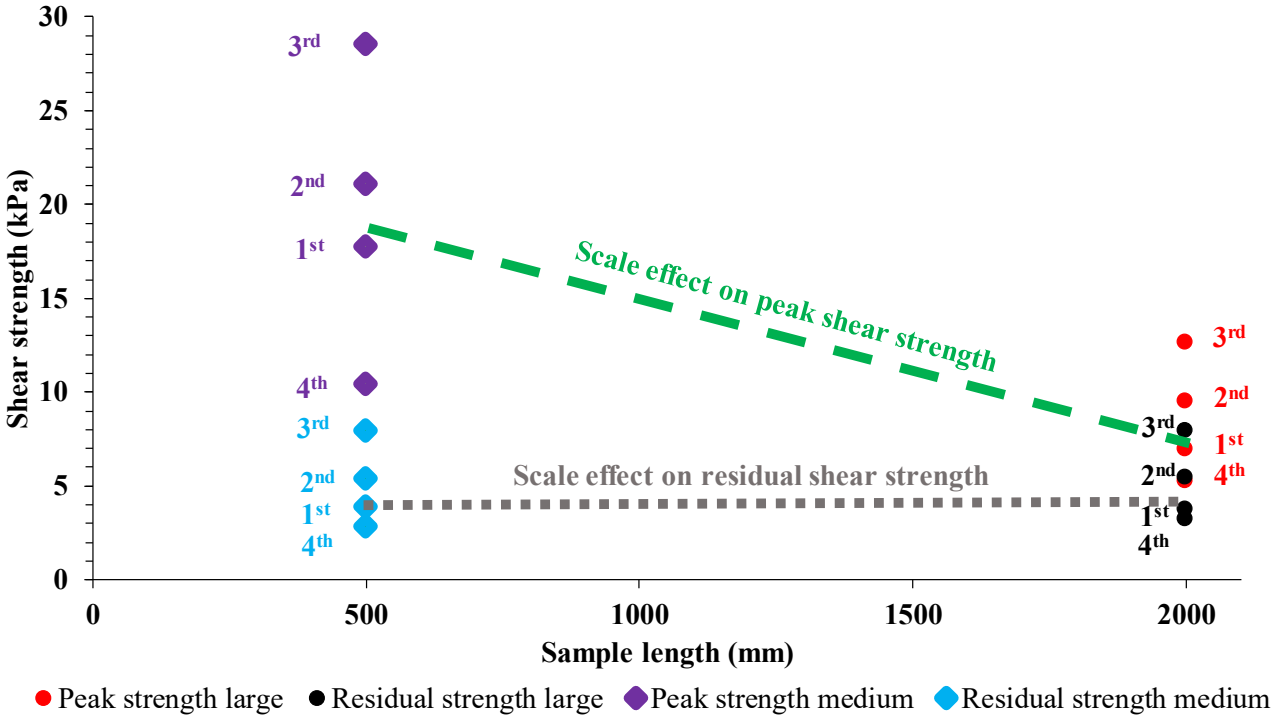

Figure 15. Peak and residual shear strength at different loading stages and scales.

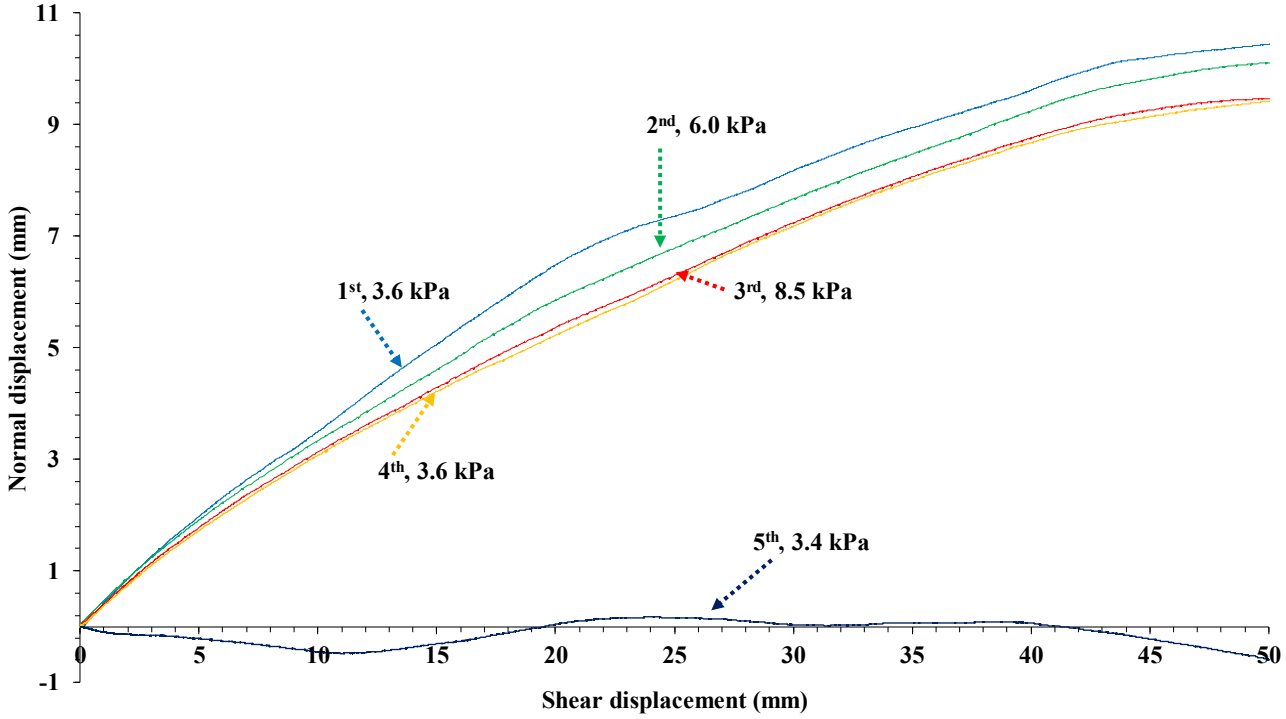

Figure 16. Average normal deformation during the shearing in each test stage of the large sample.

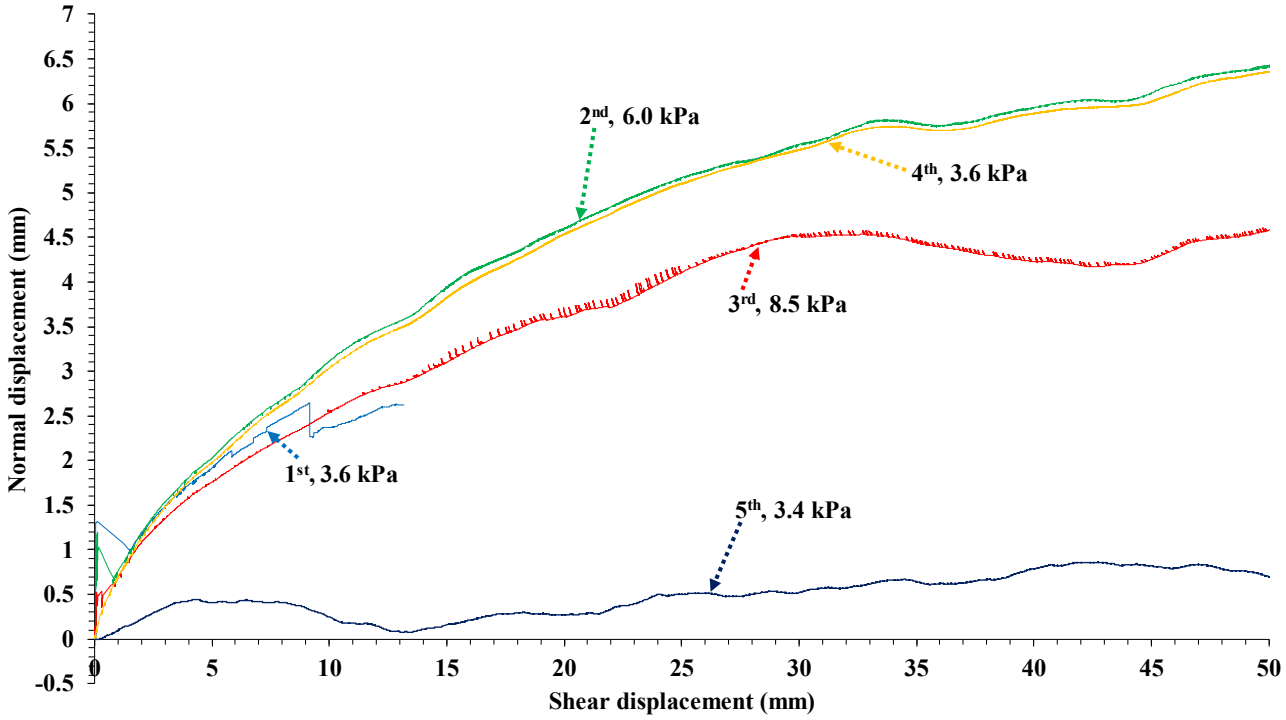

Figure 17. Average normal deformation during the shearing in each test stage of the medium sample.

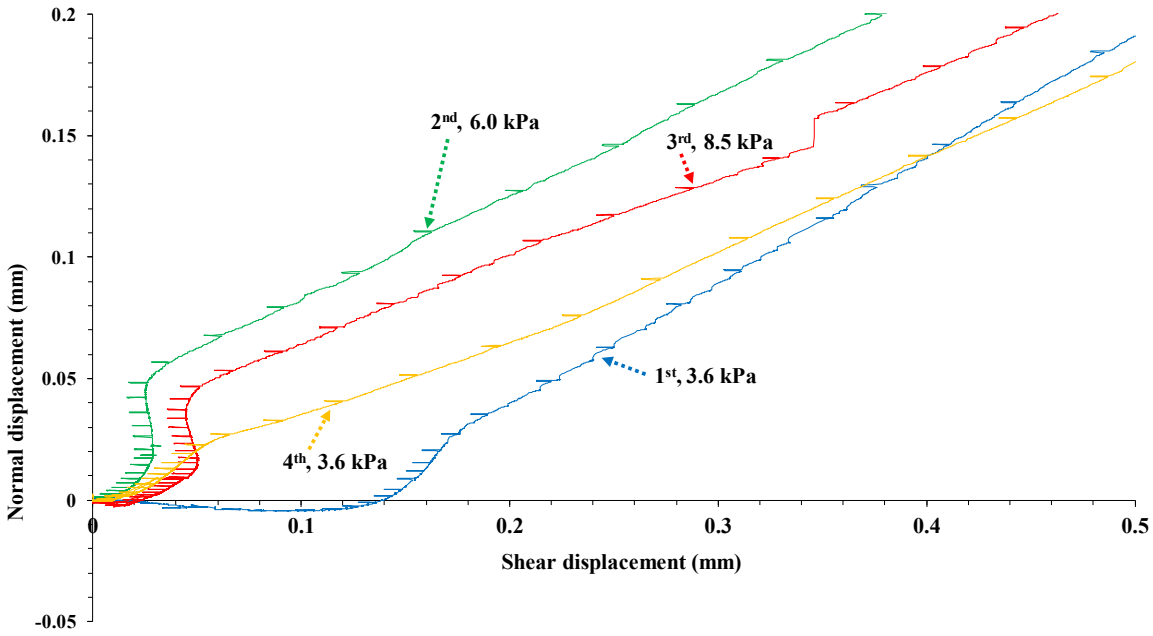

Figure 18. Transition from negative to positive values of dilation during the different stages of the large push shear test.

Table 3. Shear test results for both the large (2000 mm × 1000 mm) and medium (500 mm × 250 mm) samples.

PHASE	Normal Stress	Large Size Sample 2000 mm × 1000 mm			Medium Size Sample 500 mm × 250 mm		
		Peak Shear Strength	Residual Shear Strength	Shear Displacement at Peak	Peak Shear Strength	Residual Shear Strength	Shear Displacement at Peak
	(kPa)	(kPa)	(kPa)	(mm)	(kPa)	(kPa)	(mm)
First stage	3.6	6.9	3.7	0.52	17.8	3.9	0.08
Second stage	6.0	9.5	5.4	0.73	21.1	5.4	0.11
Third stage	8.5	12.0	7.9	0.68	28.6	8.0	0.07
Fourth stage	3.6	5.2	3.2	0.50	10.4	2.8	0.10
Fifth stage	3.4	N/A	2.05	60.0	N/A	2.5	1.18

The shear displacement of the sample and the resultant shear strength are represented in the positive portion of the x-axis. The peak and residual envelopes are represented on the negative portion of the x-axis according to the normal stress applied. A non-linear relationship between the normal stress and the shear strength is seen for both envelopes. This non-linearity is more prominent in the first part of the curves. Figure 12a presents some downward spikes regarding the stick-slip phenomenon after the peak shear strength was achieved; this effect was also previously reported for the pulling test [49,54]. During the loading, the pistons apply incremental force until the friction opposed by the surface's roughness is overcome, resulting in shear displacement and a sudden drop in the force registered by the sensors, then building up until again reaching the limit of frictional resistance. This process was repeated several times until 2.5% of the sample length (5 cm for the large sample and 1.25 cm for the medium sample) was reached. From the results obtained and shown in Figure 12a, increasing normal stress the peak shear strength requires larger elastic deformation and displacement to reach the peak (Table 3). The shear strength profile for stage 4 presents a lower peak compared to stage 1 with the same normal stress. Additionally, the resulting curve seems more homogeneous than the previous stages, possibly meaning that the bigger asperities on the surface opposing the displacement in the previous stages have been crushed, and the sliding is smoother.

The peak shear strength was achieved before 1 mm of shear displacement for every loading stage. As the normal stress was increased, so was the shear displacement necessary

to reach the peak strength. Once the extra pressure was taken away from the samples, the displacement required to reach the peak dropped again, as shown in Table 3.

Similarly, Figure 13a illustrates the results of the shearing test on the medium sample. Figure 13b shows the shear strengths before the peaks (Table 3). In terms of the peak and residual envelopes, the results present a similar linear relationship as for the large sample (Figures 14 and 15). The results are consistent between both tests; with increasing normal stress, the resulting shear stress increases. Nonetheless, it is not the case of the shear displacement required to achieve peak shear strength, as shown in Table 3. In both cases, the shear displacement to achieve the peak shear strength increased from stage 1 to stage 2, while it decreased during stage 3.

The normal stresses used in both large and medium sample tests were low compared to the expected normal stresses hundreds of meters deep underground. The comparison between the results for both samples is illustrated in Figures 14 and 15. The peak and residual strengths from the large test show a clear linear correlation between the shear strength and the normal stress applied. The coefficient of determination R^2 for the peak strength is 0.95 and for the residual strength 0.98 (Figure 14).

Furthermore, in the medium test, the linear correlation seen in the large sample is consistent in the resultant residual strength at the different stages with a determination coefficient of 0.99. The peak shear strength for the medium sample does not show such a high degree of determination (0.84). The peak shear strength for the fourth stage of the medium test represented 58% of the shear strength achieved during the first stage. In contrast, in the large sample, this same relation was only 25%. The linear Mohr–Coulomb failure criteria were fitted to all the results obtained from the large and medium samples and both peak shear and residual shear strengths (Figure 14). The approximated characteristics of the mechanical properties of the rock fractures, cohesion, and friction angle are summarized in Table 4.

Table 4. Cohesion and friction angle according to Mohr–Coulomb failure criteria from the shear test.

Sample	Peak Friction Angle (°)	Peak Cohesion (kPa)	Residual Friction Angle (°)	Residual Cohesion (kPa)
Large sample (2000 mm × 1000 mm)	53.34	1.27	41.9	0.217
Medium sample (500 mm × 250 mm)	71.19	3.51	42.72	0.028

As shown in Table 4, the scale effect does not exist in the residual friction angle. In contrast, the peak friction angle for the large test (53°) is reduced to almost 75% of the medium test result (71°) and the peak cohesion of the large test (1.3 kPa) is reduced to 36% of the medium test result (3.5 kPa).

The peak strengths and residual strengths are illustrated in Figure 15. The difference in the values of the residual strength is not significant. The peak shear strength values registered for the large sample represent 39%, 45%, 44%, and 50% of the medium sample peak shear strength for stages 1 to 4, respectively (Table 3). On the other hand, the residual strength showed a contrary behavior, with a proportion (large/medium) for residual shear strength of 95%, 100%, 100%, and 114% for stages 1 to 4, respectively (Table 3). With increasing sample size, the shear strength is reduced. Nevertheless, the relationship between the residual shear strength and the sample scale does not follow the same trend.

Suppose the degree of matedness for fresh, unfilled, and rough rock fractures is decreased and the number of contact points reduced. In that case, a decrease in the mean peak shear strength is expected due to a reduction of the larger asperities opposing the shearing [14]. This effect can be seen with the reduced peak shear strength of stages 1 and 4 under the same normal stress. Additionally, the matedness effect can be observed in the dilation curves of the different stages, with a special remark on the fifth stage of both samples. For the fifth stage, the slab was turned through 180 degrees, with the aim being

to reach the lowest matedness coefficient, and then pushed along the long side as in the previous stages. As the top slab was rotated 180 degrees, the matedness of the surfaces was practically zero. During the large test, the lateral restraints of the shearing slab (top sample) had to be removed to allow transversal movement or a yaw in-plane rotation effect of the top slab while sliding over its bottom counterpart. The absence of the restraints resulted in a slightly (−0.2 kPa) lower normal stress during stage 5 and some yaw effect during the test.

Nevertheless, both the variation in the normal stress (−0.2 kPa) and the yaw effect were minimal; the top sample remained relatively straight even without the restraints. Finally, during the fifth stage, the slab was pushed until it reached 100 mm (10% of the length of the sample) for a more reliable zero matedness effect on the test. Because of the length of the test, an additional shearing rate to the normal testing rates was used for stage 5; 0.1 mm/min up to a 3.0 mm displacement, 0.5 mm/min until a 50 mm displacement, and 1.0 mm/min for the remaining 50 mm of shearing. Due to lack of matedness, the stick-slip phenomena was less prominent in the 5th stage.

For the fifth stage with the medium sample, the normal stress was set to match the 3.4 kPa used on the large sample. No further changes were made to the shear box setup for this scale, which reduced the probability of the yaw effect as lateral restraints were in place. The average normal displacement of the large sample during the shearing of the top slab was 9.86 mm after the 50 mm movement in the shearing direction. Since the pushing occurred in the uphill direction, the front sensors (S_5 and S_6 in Figure 5b) registered readings 0.7–1.0 mm higher than the rear sensors (S_3 and S_4 in Figure 5b). For the large sample, the elevation difference was 14.9 mm uphill over 2000 mm or 0.43°, and for the medium sample the elevation difference was 2.3 mm uphill over 500 mm or 0.26°. Considering that almost every single natural joint set encloses certain inclination degrees of its shearing plane (joint surfaces) regarding the shearing direction [69], a correction of the dilation data for the large test was performed to account for the influence of the slope effect. The same correction was applied in evaluating the dilation results of the medium sample, which also sheared uphill. Figures 16 and 17 present the adjusted curves of dilation phenomena for the large and medium slabs, respectively, once the uphill effect had been corrected.

During the large test, the dilation curve of the rock was as expected. The normal displacement curves kept growing at a reducing pace until almost reaching the point at which the curves start to flatten, at 50 mm horizontal displacement. The observed average dilation decreased with every shearing stage as the asperities opposing the greater resistance to displacement were becoming crushed (Figure 16). The additional weight placed on top of the slab also contributed to the crushing of the asperities, as observed by a drop in the height of the curves after each stage, but especially in the gap between the curves of stages 1 and 4 under the same normal stress. In stage 5, the dilation presents a negative value for a large part of the experiment, corresponding to the low or non-existent degree of matedness between the surfaces and the open character of the fracture. This phenomenon was also reported in [58]. They concluded that fractures with large apertures have the lowest shear strength since the matedness of such fractures is poorer, i.e., fewer resistance contact points.

In contrast to the normal stress–dilation relationship of the large sample, the medium sample showed an odd response (Figure 17). The stage 1 normal displacement was partially lost due to incorrect sensor reset and maxing out of S_7, S_8, S_9, S_{10}. At the beginning of the shearing, and consistently for stages 1 to 4, but most noticeably in stages 1 and 2, the dilation recorded for the top slab went up quickly with a sudden drop and fast axial displacement, corresponding to the moment when the peak shear strength was overcome. After this point, the dilation continued with an increasing trend as in the large case. While the dilation decreased with increasing normal stress and shearing stage in the large test, this statement did not become a tendency for the medium sample. Figure 17 shows there was no correlation between the normal stress applied and the dilation. With increasing

normal stress and shearing stages, the bigger asperities on the fracture surface should be crushed, reducing their height and the displacement-opposing surface area. This is consistent with the quasi-identical curves of stages 2 and 4, where the results are similar to the large case.

In contrast to the trend seen in the fifth stage in the large test, the fifth stage in the medium test shows increasing dilation with the highest degree of matedness. This result can be explained by the differences in the shear apparatus setup. Since the medium slab fitted onto a shear box, the surrounding frame provided the lateral restraint of the top slab, preventing the yaw effect to a maximum degree.

Finally, as the same normal stress was applied on the rock surface with a smaller area opposing the shear displacement, the shear strength resulted in higher values that could have crushed the bigger asperities in the samples' surfaces sooner, resulting in smaller dilation values. The medium test shows about half of the dilation observed in the end phase of the test compared to the large test. In addition, it is noteworthy that every rock fracture is different. Therefore, the surface profile of both samples is not the same and could vary in a high degree between them, i.e., the height, extent, and distribution of the asperities in the surface of the slabs could be quite different, between sample, even if extracted from the same rock domain.

Figure 18 illustrates the transition point from negative to positive values in the dilation experienced by the large top slab at each stage first to fourth of the shear test. The transition at each stage occurs before the slab has been displaced by 0.15 mm. As a technical note, the reversed shearing of 2nd and 3rd tests in Figure 18 are most likely some effects of the loading configuration and the sample support system and should be not interpreted as a part of the measured signal but more as loading start artefacts. The top block was well placed and matched over the bottom sample at each stage since the transition from negative to positive dilation took very little shear displacement to occur. The contrary effect was explained in [48], where the pull test resulted in a significant negative-to-positive transition in dilation at greater sheared distances, leading to a special observation about the probability of an existing mismatch at the beginning of the stages because of bad positioning. Therefore, the top part of the sample makes micro-adjustments as the shearing force is increased until the matching position, represented by the negative part of the dilation curve, is found and the surfaces are locked in position. Subsequently, the asperities are overrun by the shear force, resulting in the vertical displacement of the top slab. From the results observed in both tests, stage 1 presented the largest shear displacement before transition from negative to positive normal displacement of the four stages. This could correspond to the fact that with every further shearing stage, the micro-scale surface asperities become crushed, and the contact surface between the rock samples evens out.

3.3. Method Comparison for Peak Friction Angles

The shear strength tests results were compared with the roughness analysis made with the profilometer and the photogrammetry measurements (Table 5). The JRC values of the direct shear tests were back-calculated with the outcomes from the first stage of the shear tests and Equation (9). The JRC values of the direct shear tests were influenced by the sample size, decreasing from 9.54 for the medium sample to 6.17 for the large-scale one by approximately 35%. The scaled JRC significantly underestimates the JRC by -28%, the scaled Z_2 method underestimates the JRC by -19%, and the Z'_2 method by -7%. The peak friction angles estimated with Equation (8) were close to the results of the shear test between 75° to 78°, except the peak friction angle predicted by Z_2, that results in 70°.

Table 5. Comparison of the peak friction angle values.

Item (Using Barton–Bandis's Criterion)			Large		Medium	
			JRC	Peak Friction Angle (°)	JRC	Peak Friction Angle (°)
Direct shear test			6.17	62.51	9.54	78.6
Profilometer	L_0		10.5	81	9.3	77
	L_{scaled}		5.6	59.8	6.9	66
Photogrammetry	Z_2	L_0	10.11	77.53	10.88	85
		L_{scaled}	5.5	59.3	7.7	69.8
	Z'_2		6.95	66.22	8.91	75.58

Regarding the large-scale sample, the scaled JRC underestimates the JRC by −9% and the scaled Z_2 method gives a result similar to the scaled JRC with −9% underestimation. The modified RMS (Z'_2) produces a result (6.95, +13%) comparable with the experimental result (6.17). The estimated JRC value by the modified RMS (Z'_2) method and the JRC from the shear test are similar (6.95 and 6.17), and the estimated peak friction angle and the experimental peak friction angles are 66.22° (+6% error) and 62.51°, respectively.

The scale correction for JRC was taken into account by Bandis et al. [3], Equation (10):

$$JRC_{scaled} = JRC_0 \left[\frac{L_{scaled}}{L_0} \right]^{-0.02JRC_0} \quad (10)$$

where JRC_{scaled} represents the scaled JRC values with different sizes rather than the 10 cm laboratory scale, JRC_0 signifies the average of JRC values of each 10 cm section, L_{scaled} refers to the length of samples, and L_0 is 10 cm.

4. Conclusions

In this research, push shear tests were conducted on two granite samples with artificially induced well-matching tensile fractures. The length and width of the fractures of the large sample were 2000 mm × 1000 mm and 500 mm × 250 mm for the medium sample. A push test was conducted at three normal stress levels of 3.6, 6.0, and 8.5 kPa for both large and medium samples. The displacement was reset for each stress level. The larger sample reached on average a −60% weaker peak shear stress than the medium sample with the same normal stress. In other words, a strong negative scale effect was observed in the peak shear strength. No scale effect was observed in the residual shear stress values, and the residual shear stress remained similar for both fracture sizes. In conclusion, neither conceptual model by Barton and Choubey [5] with a −33% reduction of the peak strength or Johansson and Stille [58], with a −0% predicted reduction of the peak strength, predicted the results correctly.

The roughness of the surfaces was measured using a profilometer and photogrammetry. The scale-corrected profilometer-based method underestimates the joint roughness coefficient (JRC) and the peak friction angle for the medium-sized slabs, with a −27% error. The photogrammetry-based Z'_2 estimate resulted in an error of −7%. For the large sample, the scale-corrected profilometer-based method leads to an underestimation of both the JRC and peak friction angle, with a −9% error. Here, the photogrammetry-based method Z'_2 produces an estimate with +12% overestimation. In conclusion, the photogrammetry-based method Z'_2 is an objective method that consistently produces usable estimates for the JRC and peak friction angle.

Author Contributions: Conceptualization, L.U.; methodology, E.C.H., L.U., M.T.; literature M.T.; software, L.U., M.T., E.C.H.; validation, L.U. and M.T.; formal analysis, M.T.; investigation, E.C.H.; resources, L.U.; data curation, E.C.H.; writing—original draft preparation, E.C.H., A.B., M.T., L.U.; writing—review and editing, M.R., A.B., L.U., M.T.; visualization, M.T. and L.U.; supervision, M.R.; project administration, L.U.; funding acquisition, L.U. All authors have read and agreed to the published version of the manuscript.

Funding: This work was made possible thanks to the funding provided by the State Nuclear Waste Management Fund (VYR) and the support of the Finnish Ministry of Economic Affairs and Employment on the Finnish Research Programme on Nuclear Waste Management KYT2018 and KYT2022 of the Nuclear Energy Act (990/1987) in the research projects Mechanical Properties of Rock Joints (KARMO) and Fluid flow in fractured hard rock mass (RAKKA).

Acknowledgments: We are thankful for the valuable comments from three anonymous reviewers which improved the manuscript. We also thank Nick Barton for taking the time to comment the preprint and suggest improvements to the manuscript.

Conflicts of Interest: The authors declare no conflict of interest.

Appendix A. Experimental

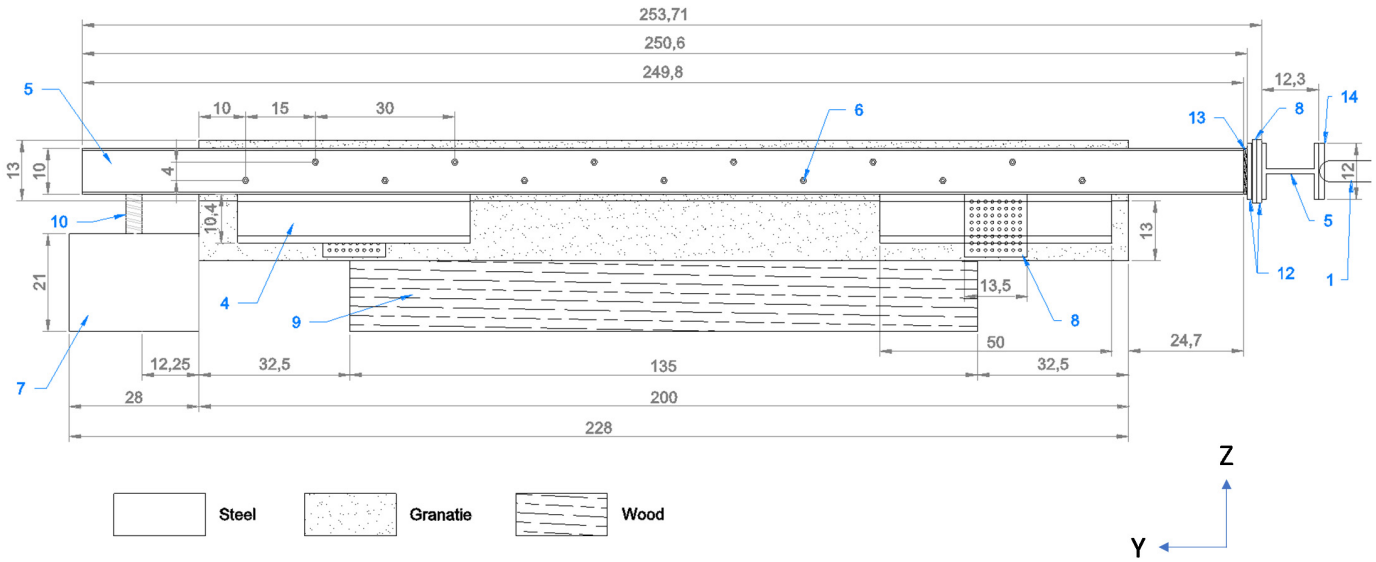

Figure A1. Side view of the experimental setup. Dimensions in centimeters [cm].

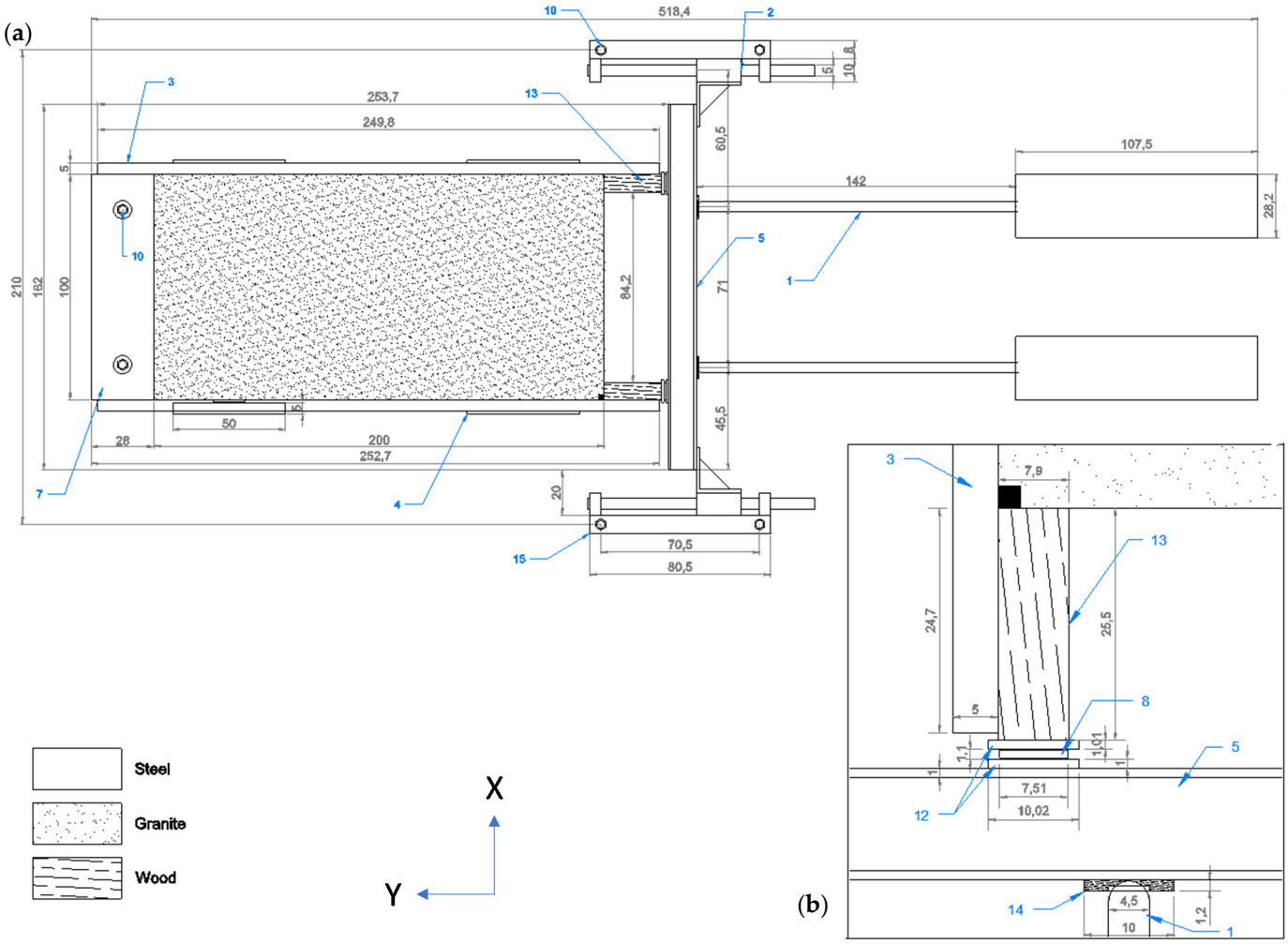

Figure A2. (**a**) Top view of the experimental setup. (**b**) Close-up of contact mechanism between the hydraulic cylinders and the rock slab. Dimensions in centimeters [cm]. 1—Hydraulic cylinders; 2—Actuators; 3—Steel beams—frame; 4—Steel beams—lateral restriction; 5—Steel beam—H-beam (force transfer); 6—Bolts; 7—Barrier; 8—Ball plates; 9—Wooden pallet; 10—Floor anchors; 11—Steel clamps; 12—Steel plates; 13—Wooden blocks—force transfer; 14—Wooden plate—centralizer; 15—Steel support—HSS profile.

References

1. Castelli, M.; Re, F.; Scavia, C.; Zaninett, A. Experimental evaluation of scale effects on the mechanical behavior of rock joints. In Proceedings of the EUROCK 2001 Rock Mechanics—A Challenge for Society, Espoo, Finland, 3–7 June 2001.
2. Bandis, S. Experimental Studies of Scale Effects on Shear Strength, and Deformation of Rock Joints. Ph.D. Thesis, University of Leeds, Leeds, UK, 1980.
3. Bandis, S.; Lumsden, A.C.; Barton, N.R. Experimental studies of scale effects on the shear behavior of rock joints. *Int. J. Rock Mech. Min. Sci. Geomech. Abstr.* **1981**, *18*, 1–21. [CrossRef]
4. Patton, F.D. Multiple modes of shear failure in rock. In Proceedings of the 1st ISRM Congress, International Society for Rock Mechanics and Rock Engineering, Lisbon, Portugal, 25 September–1 October 1966.
5. Barton, N.; Choubey, V. The shear strength of rock joints in theory and practice. *Rock Mech.* **1977**, *10*, 1–54. [CrossRef]
6. Zhao, J. Joint surface matching and shear strength part A: Joint matching coefficient (JMC). *Int. J. Rock Mech. Min. Sci.* **1997**, *34*, 173–178. [CrossRef]
7. Zhao, J. Joint surface matching and shear strength part B: JRC-JMC shear strength criterion. *Int. J. Rock Mech. Min. Sci.* **1997**, *34*, 179–185. [CrossRef]
8. Cruden, D.M.; Hu, X.Q. Basic friction angles of carbonate rocks from Kananaskis country, Canada. *Bull. Int. Assoc. Eng. Geol.* **1988**, *38*, 55–59. [CrossRef]
9. Barton, N. The shear strength of rock and rock joints. *Int. J. Rock Mech. Min. Sci. Geomech. Abstr.* **1976**, *13*, 255–279. [CrossRef]
10. Ulusay, R.; Karakul, H. Assessment of basic friction angles of various rock types from Turkey under dry, wet and submerged conditions and some considerations on tilt testing. *Bull. Eng. Geol. Environ.* **2016**, *75*, 1683–1699. [CrossRef]

11. Özvan, A.; Dinçer, İ.; Acar, A.; Özvan, B. The effects of discontinuity surface roughness on the shear strength of weathered granite joints. *Bull. Eng. Geol. Environ.* **2014**, *73*, 801–813. [CrossRef]
12. Brown, S.R. Fluid flow through rock joints: The effect of surface roughness. *J. Geophys. Res. B Solid Earth* **1987**, *92*, 1337–1347. [CrossRef]
13. Cravero, M.; Iabichino, G.; Piovano, V. Analysis of large joint profiles related to rock slope instabilities. In Proceedings of the 8th ISRM Congress, International Society for Rock Mechanics and Rock Engineering, Tokyo, Japan, 25 September 1995.
14. Johansson, F. Influence of scale and matedness on the peak shear strength of fresh, unweathered rock joints. *Int. J. Rock Mech. Min. Sci.* **2016**, *82*, 36–47. [CrossRef]
15. Barton, N. Review of a new shear-strength criterion for rock joints. *Eng. Geol.* **1973**, *7*, 287–332. [CrossRef]
16. Serasa, A.S.; Lai, G.T.; Rafek, A.G.; Hussin, A. Peak friction angle estimation from joint roughness coefficient of discontinuities of limestone in Peninsular Malaysia. *Sains Malays.* **2017**, *46*, 181–188. [CrossRef]
17. Rafek, A.G.; Lai, G.T.; Serasa, A.S. A Low Cost Alternative Approach to Geological Discontinuity Roughness Quantification. In *IAEG/AEG Annual Meeting Proceedings, San Francisco, California*; Springer: Cham, Switzerland, 2019.
18. Tse, R.; Cruden, D.M. Estimating joint roughness coefficients. *Int. J. Rock Mech. Min. Sci. Geomech. Abstr.* **1979**, *16*, 303–307. [CrossRef]
19. Maerz, N.H.; Franklin, J.A.; Bennett, C.P. Joint roughness measurement using shadow profilometry. *Int. J. Rock Mech. Min. Sci. Geomech. Abstr.* **1990**, *27*, 329–343. [CrossRef]
20. Tatone, B.S.; Grasselli, G. A new 2D discontinuity roughness parameter and its correlation with JRC. *Int. J. Rock Mech. Min. Sci.* **2010**, *47*, 1391–1400. [CrossRef]
21. Zhang, G.; Karakus, M.; Tang, H.; Ge, Y.; Zhang, L. A new method estimating the 2D joint roughness coefficient for discontinuity surfaces in rock masses. *Int. J. Rock Mech. Min. Sci.* **2014**, *72*, 191–198. [CrossRef]
22. Magsipoc, E.; Zhao, Q.; Grasselli, G. 2D and 3D Roughness Characterization. *Rock Mech. Rock Eng.* **2020**, *53*, 1495–1519. [CrossRef]
23. Brown, S.R.; Scholz, C.H. Broad bandwidth study of the topography of natural rock surfaces. *J. Geophys. Res. B Solid Earth* **1985**, *90*, 12575–12582. [CrossRef]
24. Thom, C.A.; Brodsky, E.E.; Carpick, R.W.; Pharr, G.M.; Oliver, W.C.; Goldsby, D.L. Nanoscale roughness of natural fault surfaces controlled by scale-dependent yield strength. *Geophys. Res. Lett.* **2017**, *44*, 9299–9307. [CrossRef]
25. Lanaro, F. A random field model for surface roughness and aperture of rock fractures. *Int. J. Rock Mech. Min. Sci.* **2000**, *37*, 1195–1210. [CrossRef]
26. Ficker, T.; Martišek, D. Digital fracture surfaces and their roughness analysis: Applications to cement-based materials. *Cem. Concr. Res.* **2012**, *42*, 827–833. [CrossRef]
27. Renard, F.; Mair, K.; Gundersen, O. Surface roughness evolution on experimentally simulated faults. *J. Struct. Geol.* **2012**, *45*, 101–112. [CrossRef]
28. Mah, J.; Samson, C.; McKinnon, S.D.; Thibodeau, D. 3D laser imaging for surface roughness analysis. *Int. J. Rock Mech. Min. Sci.* **2013**, *58*, 111–117. [CrossRef]
29. Fardin, N.; Feng, Q.; Stephansson, O. Application of a new in situ 3D laser scanner to study the scale effect on the rock joint surface roughness. *Int. J. Rock Mech. Min. Sci.* **2004**, *41*, 329–335. [CrossRef]
30. Sagy, A.; Brodsky, E.E.; Axen, G.J. Evolution of fault-surface roughness with slip. *Geology* **2007**, *35*, 283–286. [CrossRef]
31. Grasselli, G.; Wirth, J.; Egger, P. Quantitative three-dimensional description of a rough surface and parameter evolution with shearing. *Int. J. Rock Mech. Min. Sci.* **2002**, *39*, 789–800. [CrossRef]
32. Tatone, B.S. Quantitative Characterization of Natural Rock Discontinuity Roughness In-Situ and in the Laboratory. Ph.D. Thesis, University of Toronto, Toronto, ON, Canada, 2009.
33. Tatone, B.S.; Grasselli, G. Use of a stereo-topometric measurement system for the characterization of rock joint roughness in-situ and in the laboratory. Rock Engineering in Difficult Conditions. In Proceedings of the 3rd CANUS Rock Mechanics Symposium, Toronto, ON, Canada, 9−15 May 2009.
34. El-Soudani, S.M. Profilometric analysis of fractures. *Metallography* **1978**, *11*, 247–336. [CrossRef]
35. Unal, M.; Yakar, M.; Yildiz, F. Discontinuity surface roughness measurement techniques and the evaluation of digital photogrammetric method. In Proceedings of the 20th international Congress for Photogrammetry and Remote Sensing (ISPRS), Istanbul, Turkey, 12−23 July 2004; pp. 1103–1108.
36. Lee, H.S.; Ahn, K.W. A prototype of digital photogrammetric algorithm for estimating roughness of rock surface. *Geosci. J.* **2004**, *8*, 333–341. [CrossRef]
37. Haneberg, W.C. Directional roughness profiles from three-dimensional photogrammetric or laser scanner point clouds. In Proceedings of the 1st Canada-US Rock Mechanics Symposium, Vancouver, BC, Canada, 27 May 2007.
38. Baker, B.R.; Gessner, K.; Holden, E.J.; Squelch, A.P. Automatic detection of anisotropic features on rock surfaces. *Geosphere* **2008**, *4*, 418–428. [CrossRef]
39. Poropat, G.V. Remote characterisation of surface roughness of rock discontinuities. In *First Southern Hemisphere International Rock Mechanics Symposium*; Potvin, Y., Carter, J., Dyskin, A., Jeffrey, R., Eds.; Australian Centre for Geomechanics: Perth, Australia, 2008; pp. 447–458. [CrossRef]
40. Poropat, G.V. Measurement of surface roughness of rock discontinuities. In Proceedings of the 3rd CANUS Rock Mechanics Symposium, Toronto, ON, Canada, 9−15 May 2009.

41. Nilsson, M.; Edelbro, C.; Sharrock, G. Small scale joint surface roughness evaluation using digital photogrammetry. In Proceedings of the ISRM International Symposium-EUROCK 2012, Stockholm, Sweden, 28 May 2012.
42. Kim, D.H.; Gratchev, I.; Balasubramaniam, A. Determination of joint roughness coefficient (JRC) for slope stability analysis: A case study from the Gold Coast area, Australia. *Landslides* **2013**, *10*, 657–664. [CrossRef]
43. Kim, D.H.; Gratchev, I.; Poropat, G.V. The determination of joint roughness coefficient using three-dimensional models for slope stability analysis. In *2013 International Symposium on Slope Stability in Open Pit Mining and Civil Engineering*; Australian Centre for Geomechanics: Perth, Australia, 2013; pp. 281–289. [CrossRef]
44. Kim, D.H.; Poropat, G.V.; Gratchev, I.; Balasubramaniam, A. Improvement of photogrammetric JRC data distributions based on parabolic error models. *Int. J. Rock Mech. Min. Sci.* **2015**, *80*, 19–30. [CrossRef]
45. Kim, D.H.; Poropat, G.; Gratchev, I.; Balasubramaniam, A. Assessment of the accuracy of close distance photogrammetric JRC data. *Rock Mech. Rock Eng.* **2016**, *49*, 4285–4301. [CrossRef]
46. Sirkiä, J.; Kallio, P.; Iakovlev, D.; Uotinen, L. Photogrammetric calculation of JRC for rock slope support design. In *Eighth International Symposium on Ground Support in Mining and Underground Construction*; Nordlund, E., Jones, T.H., Eitzenberger, A., Eds.; Ground Support: Luleå, Sweden, 2016.
47. Iakovlev, D.; Sirkiä, J.; Kallio, P.; Uotinen, L. Determination of joint mechanical parameters for stability analysis in low stress open pit mines. In Proceedings of the 7th International Symposium on In-Situ Rock Stress, Tampere, Finland, 10–12 May 2016; Johansson, E., Raasakka, V., Eds.; Suomen Rakennusinsinöörien Liitto: Tampere, Finland, 2016.
48. Dzugala, M. Pull Experiment to Validate the Photogrammetrically Predicted Friction Angle of Rock Discontinuities. Master's Thesis, Aalto University, Espoo, Finland, 2016.
49. Dzugala, M.; Sirkiä, J.; Uotinen, L.; Rinne, M. Pull experiment to validate photogrammetrically predicted friction angle of rock discontinuities. *Procedia Eng.* **2017**, *191*, 378–385. [CrossRef]
50. Kim, D.H.; Lee, C.H.; Balasubramaniam, A.; Gratchev, I. Application of data mining technique to complement photogrammetric roughness data. In Proceedings of the 20th SEAGC—3rd AGSSEA Conference in conjunction with 22nd Annual Indonesian National Conference on Geotechnical Engineering, Jakarta, Indonesia, 6–7 November 2018.
51. Bizjak, K.F.; Geršak, A. Quantified joint surface description and joint shear strength of small rock samples. *Geologija* **2018**, *61*, 25–32. [CrossRef]
52. Pitts, A.D.; Salama, A.; Volatili, T.; Giorgioni, M.; Tondi, E. Analysis of fracture roughness control on permeability using sfm and fluid flow simulations: Implications for carbonate reservoir characterization. *Geofluids* **2019**, *2019*, 4132386. [CrossRef]
53. Uotinen, L.; Janiszewski, M.; Baghbanan, A.; Caballero Hernandez, E.; Oraskari, J.; Munukka, H.; Szydlowska, M.; Rinne, M. Photogrammetry for recording rock surface geometry and fracture characterization. In Proceedings of the ISRM International Congress on Rock Mechanics and Rock Engineering, Foz do Iguaçu, Brazil, 13–18 September 2019; CRC Press: Iguassu Falls, Brazil, 2019.
54. Uotinen, L. Prediction of Stress-Driven Rock Mass Damage in Spent Nuclear Fuel Repositories in Hard Crystalline Rock and in Deep Underground Mines. Ph.D. Thesis, Aalto University, Espoo, Finland, 2018.
55. Fardin, N.; Stephansson, O.; Jing, L. The scale dependence of rock joint surface roughness. *Int. J. Rock Mech. Min. Sci.* **2001**, *38*, 659–669. [CrossRef]
56. Tatone, B.S.; Grasselli, G. An investigation of discontinuity roughness scale dependency using high-resolution surface measurements. *Rock Mech. Rock Eng.* **2013**, *46*, 657–681. [CrossRef]
57. Bahaaddini, M.; Hagan, P.C.; Mitra, R.; Hebblewhite, B.K. Scale effect on the shear behavior of rock joints based on a numerical study. *Eng. Geol.* **2014**, *181*, 212–223. [CrossRef]
58. Johansson, F.; Stille, H. A conceptual model for the peak shear strength of fresh and unweathered rock joints. *Int. J. Rock Mech. Min. Sci.* **2014**, *69*, 31–38. [CrossRef]
59. Bost, M.; Mouzannar, H.; Rojat, F.; Coubard, G.; Rajot, J.P. Metric Scale Study of the Bonded Concrete-Rock Interface Shear Behavior. *KSCE J. Civ. Eng.* **2019**, *24*, 390–403. [CrossRef]
60. Azinfar, M.J.; Ghazvinian, A.H.; Nejati, H.R. Assessment of scale effect on 3D roughness parameters of fracture surfaces. *Eur. J. Environ. Civ. Eng.* **2019**, *23*, 1–28. [CrossRef]
61. Wang, S.; Masoumi, H.; Oh, J.; Zhang, S. *Scale-Size and Structural Effects of Rock Materials*; Woodhead Publishing: Sawston, UK, 2020.
62. Swan, G.; Zongqi, S. Prediction of shear behavior of joints using profiles. *Rock Mech. Rock Eng.* **1985**, *18*, 183–212. [CrossRef]
63. Rasilainen, K. The Finnish Research Programme on Nuclear Waste Management (KYT) 2002–2005. VTT Technical Research Centre of Finland. 2006. Available online: http://www.vtt.fi/inf/pdf/tiedotteet/2006/T2337.pdf (accessed on 27 March 2021).
64. Uotinen, L.; Torkan, M.; Janiszewski, M.; Baghbanan, A.; Nieminen, V.; Rinne, M. Characterization of hydro-mechanical properties of rock fractures using steady state flow tests. In Proceedings of the ISRM International Symposium-EUROCK 2020, Trondheim, Norway, 12–14 October 2020; Li, C.C., Odegaard, H., Hoien, A.H., Macias, J., Eds.; International Society for Rock Mechanics and Rock Engineering: Trondheim, Norway, 2020.
65. Sirkiä, J. Requirements for Initial Data in Photogrammetric Recording of Rock Joint Surfaces. Master's Thesis, Aalto University, Espoo, Finland, 2015.
66. Wu, C. VisualSFM: A Visual Structure from Motion System. 2011. Available online: http://ccwu.me/vsfm/doc.html (accessed on 14 April 2021).

67. Girardeau-Montaut, D. *CloudCompare*; EDF R&D Telecom: Paris, France, 2016.
68. Muralha, J.; Grasselli, G.; Tatone, B.; Blümel, M.; Chryssanthakis, P.; Yujing, J. ISRM suggested method for laboratory determination of the shear strength of rock joints: Revised version. *Rock Mech. Rock Eng.* **2014**, *47*, 291–302. [CrossRef]
69. Buocz, I.; Rozgonyi-Boissinot, N.; Török, Á. The angle between the sample surface and the shear plane; its influence on the direct shear strength of jointed granitic rocks and Opalinus Claystone. *Procedia Eng.* **2017**, *191*, 1008–1014. [CrossRef]